Canonical Strangeness Conservation in the Hadron Gas Model of Relativistic Heavy Ion Collisions

Sahal Yacoob

September 2001

A thesis presented to the University of Cape Town in fulfilment of the requirements for the degree of Master of Science in Theoretical Physics

Abstract

The CERN WA97 results display a strong strangeness enhancement at mid-rapidity which is dependent on the strangeness of the particle concerned, and saturates at values of participating nucleons greater than 120. These results are phenomenologically described by the mixed canonical ensemble, with canonical (exact) strangeness conservation involving all strange resonances, and grand canonical conservation of charge and baryon number. It is shown that the data are well described by an equilibrium hadron gas. Other explanations of these data are reviewed.

'Nothing is rich but the inexhaustible wealth of nature. She shows us only surfaces, but she is (a) million fathoms deep.'

– Emerson (1803–1882)

Contents

List of Tables v
List of Figures x
Conventions and Abbreviations xi

1 The Search for a Quark Gluon Plasma **1**
1.1 Introduction to Relativistic Heavy Ion Collisions 1
1.2 Thermodynamical Equilibrium 3
1.3 Signals of QGP Formation 4
1.3.1 Direct Photons and Dileptons 4
1.3.2 J/ψ Suppression 10
1.3.3 Pion Interferometry 12
1.3.4 Strangeness Enhancement 13
1.4 Aims of this Thesis 21

2 CERN WA97 **23**
2.1 The Data 23
2.1.1 Determination of the Number of Wounded Nucleons . . 25
2.1.2 Transverse Mass Spectra 26
2.1.3 Determination of Particle Multiplicities 28
2.2 How this Data has been Explained 29
2.2.1 VENUS, RQMD and UrQMD 30
2.2.2 String Fusion Model 32
2.2.3 String Fragmentation (LUCIAE) 33
2.2.4 Improved Dual Parton Model 35
2.2.5 HIJING $B\overline{B}$ 35
2.2.6 Thermal Models 36
2.2.7 A Comment on these Models 39

3 A Mixed Canonical Ensemble **41**
3.1 Theoretical Formalism 41
3.1.1 Grand Canonical Formalism 42
3.1.2 Exact Strangeness Conservation 45

3.2 Implementation 49
3.2.1 Analysis A 50
3.2.2 Analysis B 51
3.2.3 Analysis C 51
3.2.4 Comment on Analyses A, B, and C 52
3.2.5 Variation of T, R, and μ_B with $< N_{wound} >$ 53
3.2.6 Reproducing Figure 2.1 56
3.2.7 Investigation of the Importance of Including All Strange Particles in the Formalism 58
3.3 Conclusion 61

A Kinematic Variables **63**
A.1 Baryon Stopping 63
A.2 Centrality 63
A.3 Rapidity and Pseudorapidity 65
A.3.1 Rapidity 65
A.3.2 Pseudorapidity 67
A.3.3 Longitudinal Flow 67
A.4 Transverse mass (m_T), Transverse momentum (p_T), and m_T-scaling 68
A.4.1 Transverse Flow 69

B The Acceptance Region of WA97 for Pb+Pb collisions **71**

List of Tables

2.1 Yields and average number of wounded nucleons measured by the WA97 experiment, where Ω_T is the sum of omega and anti-omega particles [62]. 29

3.1 Parameters obtained for various analyses as described in the text. The temperature (T) and chemical potential (μ_B) are in MeV. The radii (R) are given in fm. If χ^2 is greater than 50, the fit parameters are not shown. 52

List of Figures

1.1 Space-time diagram of the longitudinal evolution of the Quark Gluon Plasma [4]. The central plateau of the hydrodynamic phase has no net baryon number (nuclear transparency), and the net baryon number of the incident nuclei is found at the longitudinal ends of the system. 2

1.2 Feynman diagram for the reaction $q + \overline{q} \rightarrow l^+ + l^-$ [6]. 5

1.3 Left panel: comparison of background, Drell-Yan and open charm decays with p+W and S+W Helios-3 dimuon data. Middle panel: mesonic reactions contributing to lepton pair final states are shown. Right panel: the background, total secondary contributions, and their sum are shown with the data from central S+W collisions [8]. 7

1.4 Comparison with the NA50 intermediate mass dimuon data. The left and right panels correspond to calculations with different assumptions of plasma lifetime, and initial temperature. The right panel includes a thermal QGP component [8]. 7

1.5 The CERN WA98 real photon invariant cross section data as a function of photon transverse momentum, compared with scaled p-A results and pQCD calculations [8]. 9

1.6 Fit of J/Ψ/DY against the energy in the zero degree calorimeter, normalised to nuclear absorption (1), assuming two sharp absorption mechanisms occurring at $E_{ZDC} = 27$ TeV and for the most central collisions [19]. 11

1.7 The ratio of J/Ψ over Drell-Yan from CERN NA50. The high E_T drop in the yield is not reproduced by this model based purely on nuclear absorption [21]. 11

1.8 The ratio of J/Ψ over Drell-Yan in a longitudinally, and transversally expanding hadron-gas. Again the high transverse energy drop is not explained by a purely hadronic model [23]. 12

1.9 Predicted $R_{\rm out}/R_{\rm side}$ for RHIC initial conditions as a function of p_T at freeze-out (symbols) and at hadronisation (lines) [29]. 14

1.10 Strange quark equilibration time τ as a function of the temperature, for gluon – gluon (long dashes), and quark – quark (short dashes) processes. The solid line considers both processes [6]. 15
1.11 Ratios of (a) K^+/π^+ and (b) K^-/π^- as a function of rapidity at 14.6 A GeV. Data from the E802 collaboration at Brookhaven National Laboratory [34]. 16
1.12 K/π ratio in Au+Au collisions as a function of energy [39]. . . 17
1.13 K^+/π^+ at mid-rapidity as a function of energy. The full line shows the results of a statistical model in complete equilibrium [41]. 18
1.14 K/π at mid-rapidity in symmetric systems. The full line shows extrapolation from p-p data [40]. 19
1.15 Comparison of mid-rapidity K^+/π^+ data from symmetric collisions as a function of the product of mid-rapidity π^+ and proton yields, with RQMD predictions, with (dashed line) and without (solid line) re-scattering [40]. 19
1.16 Predicted strange antibaryon yields at mid-rapidity as a function of collision centrality [42]. 20

2.1 The CERN WA97 data - Particle ratios at mid-rapidity per event per wounded nucleon relative to the p+Be yields [62]. . 24
2.2 WA97 detector set-up [62]. 24
2.3 Wounded Nucleon Model fit to the multiplicity distribution. The four multiplicity classes used in the data analysis of the Pb+Pb collisions are indicated [58]. 25
2.4 Mass dependence of the inverse slopes for the most central Pb+Pb events measured by CERN WA97 [55]. The y-axis corresponds to T_{eff} in Equation A.9. 26
2.5 Slope parameters for strange particles in 4 centrality bins measured by CERN WA97 [55]. 27
2.6 Comparison of Venus, and RQMD calculations with CERN WA97 data for p+Pb (left) and the most cental Pb+Pb (right) systems [59]. 31
2.7 Comparison of the UrQMD model with the CERN WA97 data [68]. Stars indicate the data, while shaded symbols represent UrQMD calculations with an increased string tension. 32
2.8 Comparison of the String Fusion Model with CERN WA97 data [70]. Dashed lines include re-scattering. 33
2.9 LUCIAE simulation predictions, compared to CERN WA97 data [71]. 34

2.10 Comparison of the Improved Dual Parton Model and CERN WA97 data [74]. 35
2.11 HIJING BB predictions compared with CERN WA97 data [76]. 36
2.12 Strange particle yields with increasing number of participating nucleons by Becattini, and Keränen [79]. 37
2.13 Strange particle yields normalised to p+Be predicted by the thermal model with canonical strangeness enhancement [50]. . 38
2.14 Comparison of the thermal model with Pb+Pb data from CERN WA97 [50]. 38

3.1 C_s - the correction factor to the grand canonical particle number expression, for exact baryon number (B), strangeness (S), and charge (Q) conservation, and exact strangeness conservation (S), for particles of strangeness one [79]. See Equation 3.30 for a definition of C_S. 50
3.2 Variation of the chemical freeze-out temperature (T) of the system with number of wounded nucleons. 54
3.3 Variation of the radius (R) of the system with the number of wounded nucleons. 55
3.4 Variation of the baryon chemical potential (μ_B) with radius. . 56
3.5 Comparison of the hadron gas model with exact strangeness conservation and CERN WA97 data for the Ω and strange anti-particles. 57
3.6 Comparison of the hadron gas model with exact strangeness conservation and CERN WA97 data for negatives and strange particles. 58
3.7 Comparison of the hadron gas model with exact strangeness conservation up to doubly strange (anti-)particles with WA97 data for the Ω and strange anti-particles. 59
3.8 Comparison of the hadron gas model with exact strangeness conservation up to doubly strange (anti-)particles with WA97 data for negatives and strange paricles. 60
3.9 Comparison of the hadron gas model with exact strangeness conservation of singly strange (anti-)particles with WA97 data. 60

A.1 Net proton distributions with (solid line) and without (dashed line) stopping [93]. 64
A.2 A schematic representation of a collision. As b increases, the collision becomes more peripheral. The most central collision will be at b=0 [58]. 65

A.3 Comparison of expected rapidity distributions, with (solid lines) and without (dashed lines) longitudinal flow to experimental data [89]. 66
A.4 m_T-spectra from CERN WA97 for negatives, and the K^0_S [55]. The K^0_S shows m_T-scaling. The h^- only exhibit m_T-scaling for m_T greater than 1 GeV/c^2. 70

B.1 The CERN WA97 acceptance regions for Λ, Ξ, Ω, $K^0{}_S$, and h^- particles formed by Pb+Pb collisions [55]. 71

Conventions and Abbreviations

A system of units is used in which $\hbar = c = k = 1$.
The z axis is chosen to run along the beam axis.
Variables specific to the field, which may be utilised in Chapters 1 – 3 are described in Appendix A.

Chapter 1

The Search for a Quark Gluon Plasma

1.1 Introduction to Relativistic Heavy Ion Collisions

A major goal for physicists since the beginning of scientific exploration has been the search for the basic building blocks of the universe. To a large extent this search involves the analysis of a known state of matter until its constituents may be determined. Along with identifying these basic building blocks, an understanding of how these objects interact is required.

As new particles have been identified, the process of identifying their constituents at a fundamental level has evolved. While the discovery of the electron is attributed to a single person[1], large research groups now work to discover new particles at multi-national organisations. The quarks and the leptons have thus far been identified as the most elementary particles which constitute matter. As such the properties of these particles are currently the subject of much research.

In order to probe the realm of elementary particles, the delicate operation of colliding two bodies at very high energy is performed. The bodies in these cases range from massless photons to heavy ions such as lead nuclei.

The focus of this work is primarily on Relativistic Heavy Ion Collisions (RHICs). The aim of such collisions is to study the phase diagram of strongly interacting matter at high temperatures and densities in the search for the Quark Gluon Plasma (QGP) [1]. The QGP is a theoretically hypothesised phase of matter, where quarks and gluons move freely over a

[1] J.J. Thompson

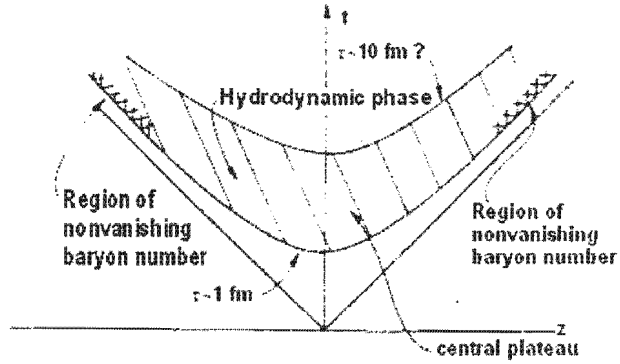

Figure 1.1: Space-time diagram of the longitudinal evolution of the Quark Gluon Plasma [4]. The central plateau of the hydrodynamic phase has no net baryon number (nuclear transparency), and the net baryon number of the incident nuclei is found at the longitudinal ends of the system.

large region of space (unlike their usual confinement within hadrons). The plasma/deconfined phase is expected to have a larger energy density than the hadronic phase. In addition, it is expected that chiral symmetry is restored in the plasma phase – dropping quark masses to zero. In a RHIC a large fraction of the energy of the collision is deposited in a small volume within a short space of time, providing an initial condition of high energy density as required for deconfinement. Two flavour lattice QCD calculations predict the critical energy density for the phase transition from hadronic matter to a deconfined Quark Gluon Plasma (QGP) phase to be $\epsilon \approx 400 - 700$ MeV/fm^3($T \approx 155 - 175$ MeV) [2]). In comparison, CERN SPS is expected to achieve an energy density $\epsilon \approx 3.5$ GeV/fm^3 in the mid-rapidity region of a symmetric central collision of ^{208}Pb nuclei [3].

If the phase transition from hadronic matter to Quark Gluon Plasma is of first order then, at the transition temperature, a mixed phase of hadron gas and deconfined plasma is hypothesised to exist. The expected space-time diagram for the evolution of a RHIC, assuming QGP formation, is shown in Figure 1.1.

The deconfined plasma phase is also of interest to cosmologists as this phase is expected to have existed at some time of order 10^{-6} seconds [4] after the big bang, when conditions were similar to those achieved in RHICs.

1.2 Thermodynamical Equilibrium

> 'A phase transition from an initial colour-deconfined QGP to a colour-confined hadronic state (as it is supposed to occur in hadronic collisions) can only be reasonably well defined if the system under study is in a state of approximate local thermodynamic equilibrium' [5].

During the initial collision a large amount of energy is deposited in a small region in space (the initial central energy density (ϵ) is estimated to be approximately $1 - 10$ GeV/fm^3 [4].). This is accompanied by the production of many secondary particles, forming a gas of elementary particles. The hypothesis of local thermodynamic equilibrium within the short lifetime of the system has been the subject of much discord. The applicability of thermal models[2] has been studied in much detail by, for example, Heinz [5] amongst others, and while no thermal model may ever truly reflect the complex dynamics of a RHIC (due to the small system, and strong dynamical evolution on time scales comparable to the microscopic thermalisation time [5]) and a deeper understanding of these exact dynamics is sought, thermal models are able to provide a rough understanding of the basic phenomena observed, and thus continue to be of use.

Within the postulates inherent in applying a thermal model, the collision system is thought to reach chemical[3] and thermal[4] equilibrium. It subsequently, or coincidentally, reaches chemical freeze-out, at which time (τ_{ch}) the particle multiplicities are frozen, according to their equilibrium thermal values (except for resonance decays to more stable states). At this stage, the assumption of chemical equilibrium ceases to be valid. From chemical to final freeze-out, the system is considered to be in thermal equilibrium. Once final freeze-out has been reached, the system ceases to exist and the individual particles may be detected. The complete evolution of the system may have a duration $\approx 5 - 10$ fm/c [4].

The picture of thermal equilibrium presented above holds where thermalisation is achieved via kinetic equilibrium (re-scattering). The statistical occupation of available phase-space has been proposed as a reason for particle distributions from lepton – lepton and nucleon – nucleon collisions appearing thermal [5]. In this scenario, particles are produced with the correct properties to fill the available phase-space, and may be regarded as having been

[2]Models which require local thermodynamic equilibrium.

[3]The densities of each species of particle may be described by thermal models with parameters $T, V,$ and μ.

[4]Particle momentum distributions may be described by thermal models.

formed already in thermal equilibrium.

1.3 Signals of QGP Formation

> 'It is generally recognised that there is no single unique signal which allows an unequivocal identification of the quark-gluon plasma phase. What can be achieved may be an accumulative set of data which taken together may indicate the presence of the deconfined phase' [6].

If formed a QGP will not be directly detectable and the best way to confirm its existence would be to predict differences between the products of a collision which has formed a QGP before hadronisation takes place and one which hasn't. A major problem is that an initial equilibrium hadron gas will be indistinguishable from a secondary equilibrium hadron gas formed from an initial QGP phase. A few suggested signals of deconfinement are described briefly below and discussed with a view to comparing current data with the initial proposal of the signal.

1.3.1 Direct Photons and Dileptons

Photons and dileptons formed during a heavy ion collision are not expected to interact with other collision products before being detected. Photons formed during the earliest times of the collision thus carry information about the initial conditions of the collision. It is a very difficult task to detect these initial collision products from the large background of photons and dileptons formed during the secondary collisions and hadronic decays which subsequently take place [7]. For a more in-depth look at this signal, see for example [8, 9].

Dilepton Production

A quark and an anti-quark from the plasma may annihilate to form a virtual photon, which then decays into a dilepton pair according to the process shown in Figure 1.2. Once formed, these leptons are required to pass through the interaction region of high baryon density. Their small cross section ($\approx \left(\frac{1}{137\sqrt{s}}\right)^2$ [6], where $\sqrt{s}$ is the centre-of-mass energy.) means that the lepton mean free path is large, and leptons are not expected to experience collisions with other particles in the interaction region before being detected.

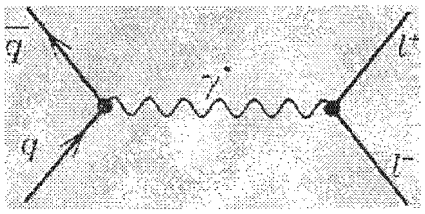

Figure 1.2: Feynman diagram for the reaction $q + \overline{q} \rightarrow l^+ + l^-$ [6].

If one is able to extract the dilepton distributions in invariant mass and rapidity, it should be possible to determine the initial temperature at which the QGP was formed [6].

In order to identify leptons formed by QGP, it is essential to understand other lepton production processes. This enables one to differentiate between leptons formed during a deconfined phase, and those formed from other interactions.

Leptons from the Drell-Yan process: (This production mechanism is important for large values of the invariant mass of a dilepton pair [6].) In nucleus – nucleus collisions, the Drell-Yan process arises from a collection of independent nucleon – nucleon interactions. In this process, a valence quark from a nucleon annihilates with a sea anti-quark from the other nucleon [6], to form a virtual photon which then decays into a dilepton. It can be shown from first order QCD calculations, that the number of dilepton formed due to the Drell-Yan process for the head-on collision of two identical nuclei is proportional to $A^{\frac{4}{3}}$ [10].

Dileptons from Hadrons and Resonances: Hadrons and resonances produced in the nucleus – nucleus collision may annihilate, or decay thereby producing dileptons. The decays of hadronic resonances will appear as sharp peaks in the invariant mass spectrum, with a width indicative of the lifetime of the resonance, and magnitude depending on the abundance of the resonance [6].

Dilepton Production from Charm Particles: The production of charm and anti-charm quarks from the QGP via virtual gluons, or a gluon – gluon interaction, leads to the formation of hadrons containing either the charm or the anti-charm quark. The decay of a meson containing a charm quark (D^+), and one containing an anti-charm quark (D^-) also gives rise to dileptons via the processes $D^+ \rightarrow$ anti-lepton + $\overline{K^0}$

and a neutrino, and $D^- \rightarrow$ lepton + K^0 and an anti-neutrino. Lowest order perturbative QCD cannot fully describe the charm production process because of the low mass of the charm quark [6], but the partons participating in charm production must have high momenta, which means that charm production occurs rarely. The dileptons produced via charm production exhibit an approximately exponential invariant mass distribution, and, at SPS Energies, are less than the number produced by the Drell-Yan process [6].

In order to be observable, the dilepton yield from a QGP must be at least of comparable magnitude to the yield from non-plasma sources. The spectrum of dileptons formed during the QGP phase is only expected to be identified in the invariant mass spectrum in the region where the invariant mass is greater than 1.5 GeV [6]. Below this region, the invariant mass spectrum is dominated by hadronic and charm meson production mechanisms, as well as the decays from the ρ, ω, and ϕ. In the region above 1.5 GeV, the dileptons from QGP are only expected to be identified if the plasma forms at an initial temperature in excess of 300 MeV [6]. At high invariant mass the multiplicity of Drell-Yan dileptons is expected to dominate due to their high effective temperature (13 - 17 GeV) [6].

The CERN Helios-3 [11] and NA38/NA50 collaborations [12] have investigated intermediate mass dileptons, as shown in Figures 1.3 and 1.4 respectively. The Helios-3 data can be satisfactorily explained by hadron gas interactions. The CERN NA50 data is best described by assuming a thermal QGP phase contributes to the dilepton yield [13]. There are, however, a large number of ambiguities in the theoretical treatment of dimuon spectra, and much work has still to be done.

Direct Photons

Photons produced in the interaction region of the collision will interact with other particles only via the electromagnetic interaction. This weak interaction implies that photons will have a long path-length and have a high probability of reaching the detectors before a secondary interaction takes place. The photon production rate and momentum distributions depend on the momentum distributions of the quarks, anti-quarks, and gluons in the plasma. Photons detected from the plasma thus give information on the thermodynamical state of the plasma at the time of their production [6]. However, the signal-to-background ratio of direct photons compared to dileptons, is smaller by roughly two orders of magnitude in heavy ion collisions [8].

The dominant process for photon production in a deconfined state is the annihilation of a quark and an anti-quark to form a photon and a gluon.

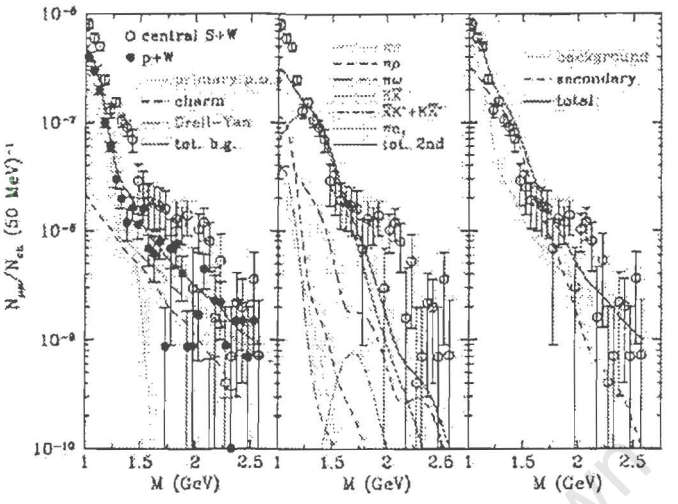

Figure 1.3: Left panel: comparison of background, Drell-Yan and open charm decays with p+W and S+W Helios-3 dimuon data. Middle panel: mesonic reactions contributing to lepton pair final states are shown. Right panel: the background, total secondary contributions, and their sum are shown with the data from central S+W collisions [8].

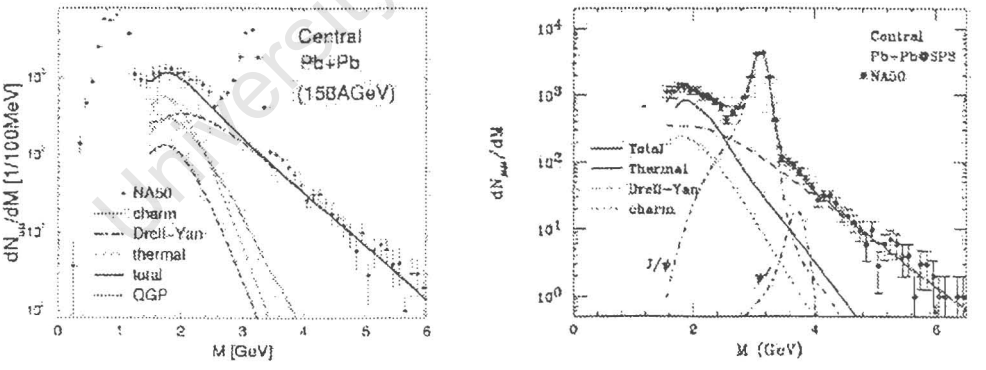

Figure 1.4: Comparison with the NA50 intermediate mass dimuon data. The left and right panels correspond to calculations with different assumptions of plasma lifetime, and initial temperature. The right panel includes a thermal QGP component [8].

This process is 50 times more likely than the annihilation of a quark and an anti-quark to form two photons [6]. The gluon – quark/anti-quark interaction producing a photon – called the Compton process – is also responsible for the production of photons in the plasma. In addition to the above first order effects, a recent QCD calculation of second order Bremsstrahlung [14] (backward scattering of a quark in the plasma) shows that the multiplicity of photons produced by this effect is of comparable magnitude to annihilation and Compton scattering multiplicities, and forms the major basis for expectations of a detectable direct photon signal of deconfinement at sufficiently high temperatures [15].

Photons are emitted by a hot hadron gas from annihilation between particle - antiparticle pairs. The hadron and plasma photon distributions are both exponential distributions of the form $e^{-E/T}$. Photons from the plasma are expected to be characterised by a higher temperature than photons formed by hadronic interactions. If the temperatures are comparable, lowest order estimates predict the spectra will be similar to each other at high photon energies [6].

CERN WA98 has reported a measurement of direct photons in ^{208}Pb+^{208}Pb collisions at 158 A GeV [16, 9]. The data along perturbative QCD (pQCD) estimates, which do not reproduce the data very well, are shown in Figure 1.5.

The CERN WA98 data show a direct photon signal above the background for transverse momenta greater than 1.5 GeV/c. The lack of data at the same centre-of-mass energy with lighter ions makes it difficult to determine if deconfinement has been achieved. Data at 200 GeV/c for proton induced reactions scaled accordingly under-predict the experimentally determined photon yield, but agree with the pQCD estimates. Hadronic explanations of the CERN WA80 data are considered untenable by Srivastava and Sinha [17], not achieving the required photon production rate. The expected QGP photon signal is shown by Srivastava and Sinha [17] to be largely independent of the transition temperature (especially at high momentum). Steffen and Thoma have recently shown, contrary to Ref. [17], that the existence of a photonic signal of QGP formation can be neither confirmed nor refuted, as there are many factors affecting the phase transition which have yet to be determined, and lead to ambiguities [18]. These include the transition temperature, and the effect that deconfinement would have on the hydrodynamical evolution of the system.

The process of photon production in elementary hadronic collisions is not yet fully understood, and this is compounded when considering nucleus - nucleus collisions. According to Gale [8], the theory has to be developed considerably before the photonic signals may be considered conclusive.

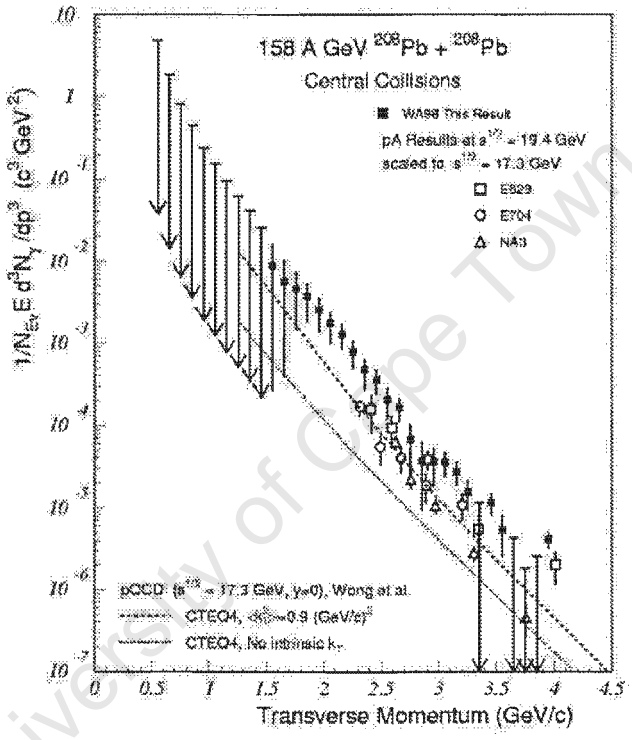

Figure 1.5: The CERN WA98 real photon invariant cross section data as a function of photon transverse momentum, compared with scaled p-A results and pQCD calculations [8].

1.3.2 J/ψ Suppression

The suppression of the J/ψ ($c\bar{c}$) has been initially proposed by Matsui and Satz [19] as a signature for QGP formation. They argued that, in a QGP, colour (Debye) screening dissolves[5] initially created J/ψ mesons into c and $\bar{c}$ quarks, which form open charm hadrons when hadronisation takes place. Thus, a suppression in the J/ψ yield (that is, a weaker A-dependence than the Drell-Yan lepton pairs) would signal QGP formation. The colour screening in the plasma modifies the long-range Coulomb-like interaction between the charm and anti-charm quarks to a short-range Yukawa-type interaction. Since the Debye screening length[6] is inversely proportional to the temperature, at high temperatures it becomes impossible for the J/ψ to form.

J/ψ suppression has been observed in oxygen on sulphur collisions at 200 A GeV[7] [20]. To account for this – and the slightly weaker A-dependence of J/ψ yields in p+A collisions – new sources of J/ψ suppression have been introduced:

Absorption in the target nucleus: This phenomenon takes place in the mid-rapidity region, where most J/ψ particles are produced, when the beam energy per nucleon is greater than 6.92 GeV [6]. There are two proposed mechanisms for the absorption of the J/Ψ in nuclear matter. One is the direct absorption of the J/Ψ particle. The other postulate assumes that even in hadronic matter a produced charm – anti-charm quark pair does not instantaneously combine to form a J/Ψ particle [21]. These quarks may interact with the nuclear medium to form open charm hadrons. In order to combine, the charm and anti-charm quarks should be produced within a distance $\approx \frac{1}{15}$ fm [21], much less than the J/Ψ diameter.

The absorption on hadronic secondaries ('comovers'): The term 'comover' refers to secondaries whose rapidity variables are close to the variables of the produced J/ψ particles. Comovers are typically ρ or ω mesons. Comoving pions don't possess the threshold energy for a reaction with the J/ψ.

The suppression measured in Pb+Pb collisions at 158 A GeV by the CERN NA50 collaboration is greater than any previously measured and cannot be accounted for by the mechanisms mentioned above [22]. This has been interpreted [20, 21, 22] as evidence for QGP formation at CERN SPS.

[5]The Debye screening weakens the interaction between the quarks, while the presence of the plasma phase ensures that the string tension goes to zero.

[6]A measure of the range of the Yukawa interaction.

[7]A system not expected t oform a QGP phase.

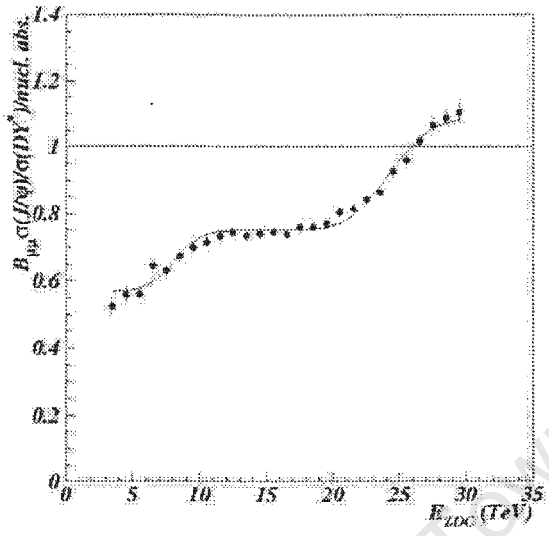

Figure 1.6: Fit of J/Ψ/DY against the energy in the zero degree calorimeter, normalised to nuclear absorption (1), assuming two sharp absorption mechanisms occurring at $E_{ZDC} = 27$ TeV and for the most central collisions [19].

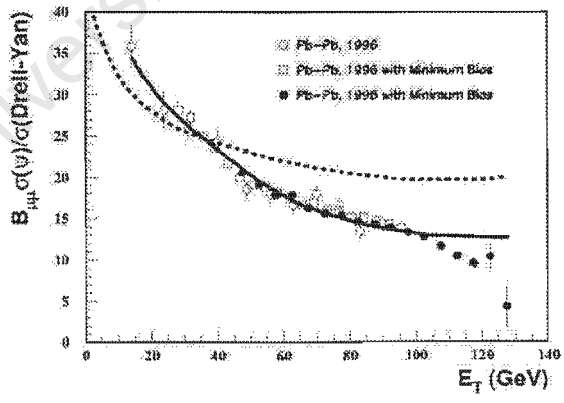

Figure 1.7: The ratio of J/Ψ over Drell-Yan from CERN NA50. The high E_T drop in the yield is not reproduced by this model based purely on nuclear absorption [21].

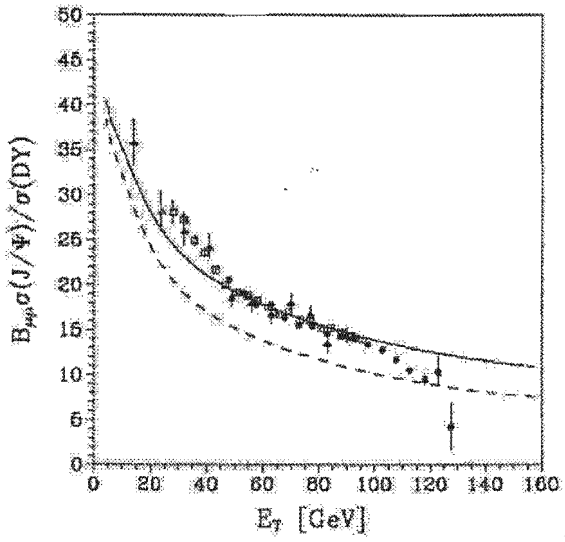

Figure 1.8: The ratio of J/Ψ over Drell-Yan in a longitudinally, and transversally expanding hadron gas. Again the high transverse energy drop is not explained by a purely hadronic model [23].

The CERN NA50 data is shown in Figures 1.6, 1.7, and 1.8. In the first figure [22], data is presented normalised to the expected values of absorption from the Glauber model [21], along with the QGP prediction which fits the data well. The next figure shows the data along with a model accounting for nuclear absorption of the charm and anti-charm quarks [21]. This model describes the data better than the Glauber model, but still fails to reproduce the anomalous J/Ψ suppression exhibited in the most central collisions at CERN NA50. The final graph shows a further attempt to describe the CERN NA50 data without assuming the formation of QGP. The analysis doesn't reproduce the data as well as the assumption of QGP in [22], and while it reproduces the most central suppression, it fails for more peripheral collisions. The analysis includes assumptions which, when modified, may reproduce the data by purely hadronic means. Presently the data from NA50 indicates the onset of new physics. Whether or not this may be attributed to the attainment of QGP, is yet to be firmly established.

1.3.3 Pion Interferometry

The phenomenon of space-time / energy-momentum correlation of identical particles emitted from an extended source is known as the Hanbury-Brown-Twiss (HBT) effect [24]. This effect is only present for chaotic sources, and

is a wave interference phenomenon based on the ratio of the probability of detecting two particles at points A and B coincidentally, to the independent probabilities of detecting particles at these two points. For coherent sources this ratio is always one. For non-coherent, or partially coherent sources, the deviation of this ratio from unity may be used to determine information about the size of the system emitting these particles. For heavy ion collisions, the interaction region may be treated as a partially chaotic source. The first pion interferometry measurement in heavy ion collisions was achieved by Fung et al. [25] for 1.8 A GeV collisions with an Ar^{40} Beam at the Lawrence Berkeley National Laboratory Bevatron on BaI_2 and Pb_3O_3 targets. The variables of interest which are brought to light by pion interferometry are the dimensions of the system in the transverse and the longitudinal directions. Pion interferometry in heavy ion collisions gives a good idea of the interaction volume, and it has been suggested [26, 27, 28] that an increase in the ratio of the transverse radius (R_{trans}) parallel to the direction of the average momentum of the detected pions to the ratio of the transverse radius (R_{out}) perpendicular to R_{trans} and the beam axis, will indicate the formation of a QGP. Soff et al. [29] show that by assuming a first order phase transition including a prolonged hadronisation time with a mixed phase, and modeling the QGP as an ideal fluid undergoing isotropic transverse expansion, it is possible to reproduce the pion interferometry data from CERN SPS at $\sqrt{s} = 17.4$ A GeV. Hydrodynamic models predict an increased R_{trans} to R_{out} ratio if a first order phase transition to deconfined matter is achieved. Ref. [29] shows that up to transverse kinetic energy ≈ 200 MeV, this ratio is independent of the critical temperature for a phase transition, as shown in Figure 1.9. A pion interferometry analysis of $\sqrt{s} = 130$ A GeV Au+Au collisions at the Relativistic Heavy Ion Collider at Brookhaven National Laboratory [30] shows an increase in system size with event multiplicity, and a decrease with transverse momentum. Ref. [30] does not, however, show any significant decrease of the R_{trans} to R_{out} ratio.

1.3.4 Strangeness Enhancement

Initially proposed by Rafelski and Müller [31], strangeness enhancement has been extensively mentioned in the literature as a signature of QGP formation. Due to the large mass of the strange (anti)quark (when compared to the u and d (anti)quarks), the equilibration time for strange particles is large compared with the lifetime of the system formed in a heavy ion collision. This phenomenon has been described in an analysis by Koch et al. [32], where the authors show, due to the large energy threshold for strange hadron pair production, that temperatures achieved in high energy heavy ion collisions

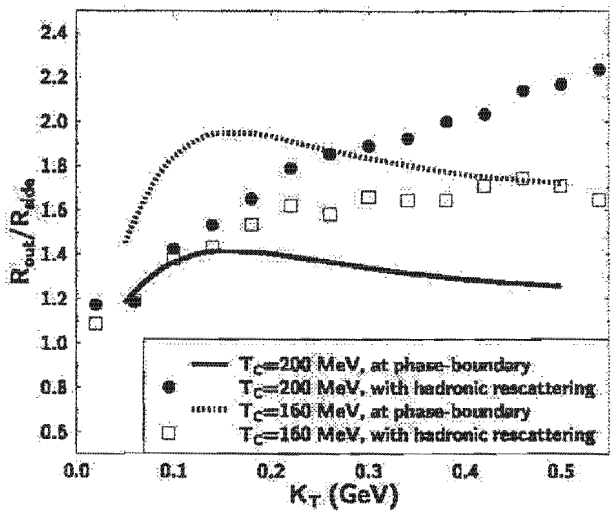

Figure 1.9: Predicted $R_{\text{out}}/R_{\text{side}}$ for RHIC initial conditions as a function of p_T at freeze-out (symbols) and at hadronisation (lines) [29].

were too low to achieve strange hadron equilibrium before the breakup of the system. Thus, the yield of strange particles detected from an initial hadronic gas state is expected to have a below-equilibrium yield of all strange particle species. If a QGP is formed, it is expected that the strange quarks rapidly equilibrate by $s\bar{s}$ pair production in the interaction of two gluons [33] which is shown to dominate light quark strangeness producing annihilations [6]. Assuming the time scale of a heavy ion collision to be in the range of $5 - 10$ fm/c, strangeness is not guaranteed to reach equilibrium, even if the deconfined state is formed. An analysis assuming massless up and down quarks, and ignoring Pauli exclusion, estimates the strange quark equilibrium time for a plasma to be ≈ 10 fm/c at 200 MeV, decreasing to a few fm/c for $T = 300$ MeV [6], as shown in Figure 1.10.

In the baryon stopping region (where the system has a net baryon number), if the deconfined phase is reached and strangeness reaches equilibrium, there will be more up and down quarks than strange and anti-strange quarks, which will in turn be more abundant than anti-up and anti-down quarks. Anti-strange quarks will then be more likely to combine with up or down quarks to form mesons $(K^0(d\bar{s}), K^+(\bar{s}u))$. Strange quarks will most likely combine with up and down quarks to form hadrons. Thus, experimental measurements of particle abundances with enhanced anti-strange mesons and strange baryons will indicate the formation of a QGP.

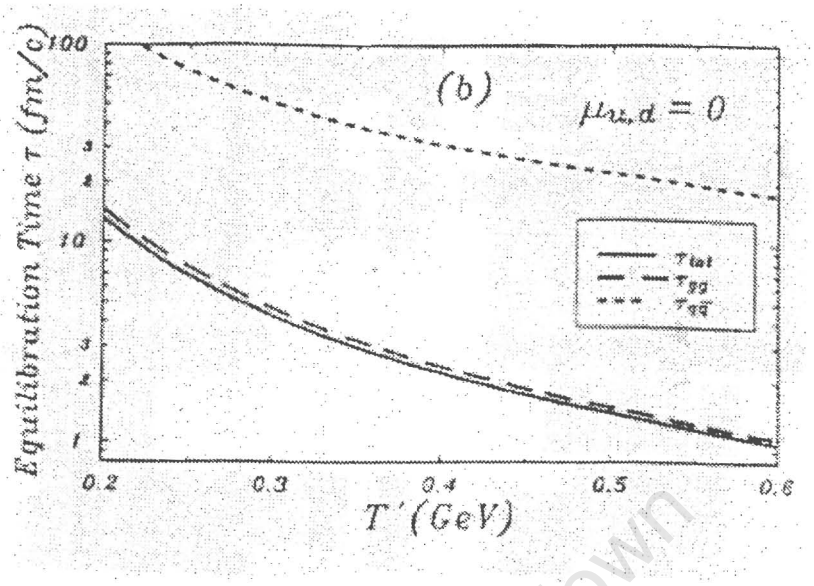

Figure 1.10: Strange quark equilibration time τ as a function of the temperature, for gluon – gluon (long dashes), and quark – quark (short dashes) processes. The solid line considers both processes [6].

Strange Meson Enhancement

Greater enhancement of the K^+/π^+ ratio than the K^-/π^- ratio has been observed by the Brookhaven National Laboratory E802 collaboration [6, 35] at the beginning of the last decade, as shown in Figure 1.11.

Alternative explanations of this phenomenon due to hadronic interactions include [35, 36, 37]. Ref. [36] explains the factor of 4 enhancement of the K^+ to π^+ ratio above it's expected extrapolation from p+p data, while the K^- to π^- remains as predicted, as an effect due to the large number of pions formed in the interaction region which subsequently decay to kaon, anti-kaon pairs. The anti-kaons K^- are then absorbed by pion producing collisions in the nuclear medium ($K^-N \leftrightarrow \Lambda\pi$).

It is important to remember that in a baryon-rich interaction region, nucleon – nucleon and pion – nucleon reactions will produce lambda's and K^0 or K^+ particles. In addition to this, K^+ particles are created by pair production, which is the only means of production of K^- particles. At the same time, K^- and $\overline{K^0}$ particles interact exothermically with nucleons to form lambda particles and pions.

More recently the E866 and E895 collaborations at the AGS have detected K^+ and K^- yields in Au+Au collisions which are under-predicted by Hadron-

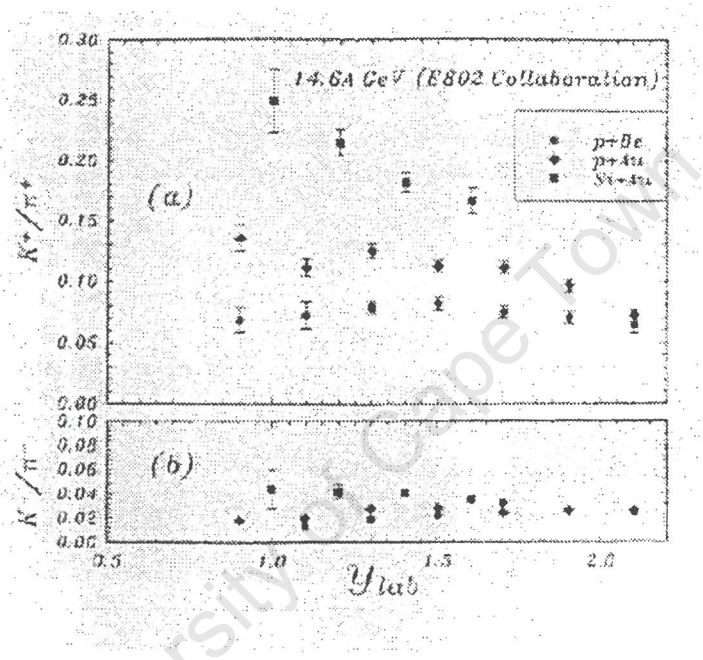

Figure 1.11: Ratios of (a) K^+/π^+ and (b) K^-/π^- as a function of rapidity at 14.6 A GeV. Data from the E802 collaboration at Brookhaven National Laboratory [34].

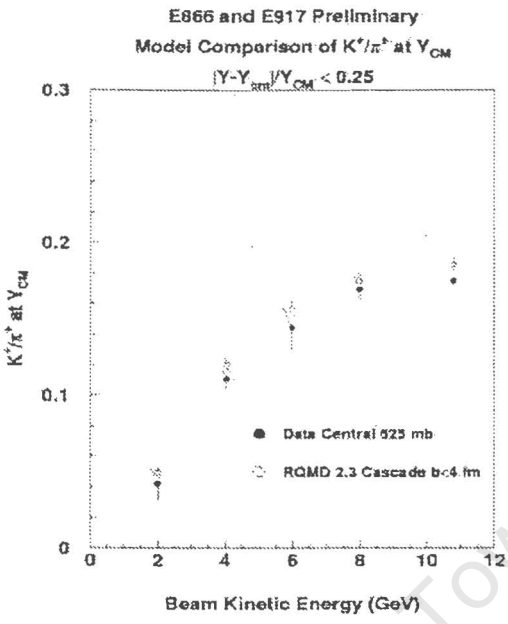

Figure 1.12: K/π ratio in Au+Au collisions as a function of energy [39].

String-Dynamics [38]. There is, in addition, an enhancement of the K^+ to π^+ ratio which is observed to increase with energy and again is not described by Hadron String Dynamics. This has led Cassing [38] to postulate the presence of non-hadronic degrees of freedom at 4 A GeV in central Au+Au collisions.

E866 and E917 preliminary data at mid-rapidity have also been well described by RQMD [39] calculations (Figure 1.12).

Cleymans, Oeschler, and Redlich [37] have shown that canonical effects in the thermal model, based on free particle masses, are sufficient to explain the E802 data, by sufficiently reproducing the K^+ and K^- yields.

The NA44 collaboration [40], in Figure 1.14, analyses the K to π ratio over a range of energies. The K^- to π^- ratio is considered to be reasonably well described by the extrapolation from p + p collisions which under-predict the K^+ to π^+ ratio. RQMD[8] (Figure 1.15) predictions over-predict the K^+ to π^+ ratio in symmetric collisions at mid-rapidity, leading the collaboration to end on the highly informative note that; 'Deconfinement scenarios of the K^+/π^+ enhancement cannot, however, be ruled out or proven by these data alone.'

Braun-Munzinger et al. [41] have shown (Figure 1.13) that mid-rapidity K^+/π^+ ratios over a range of energies are well described by fully integrated

[8] explained in Chapter2

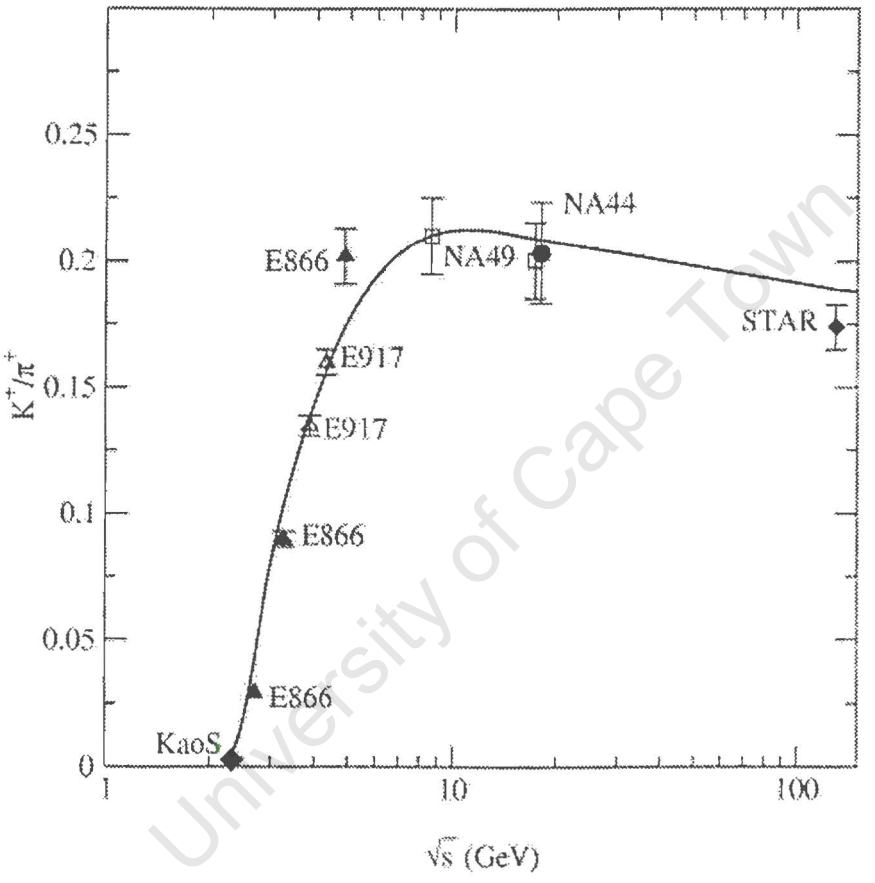

Figure 1.13: K^+/π^+ at mid-rapidity as a function of energy. The full line shows the results of a statistical model in complete equilibrium [41].

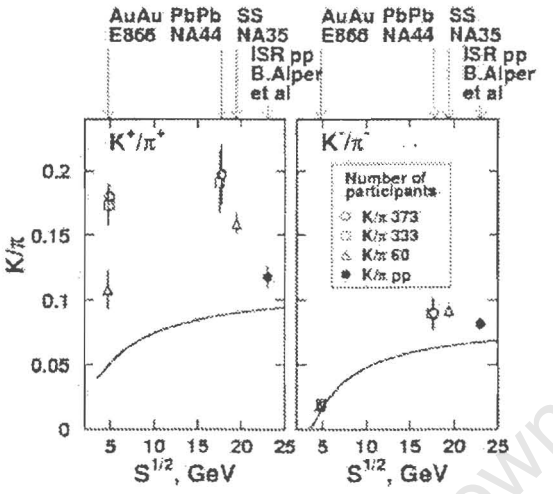

Figure 1.14: K/π at mid-rapidity in symmetric systems. The full line shows extrapolation from p-p data [40].

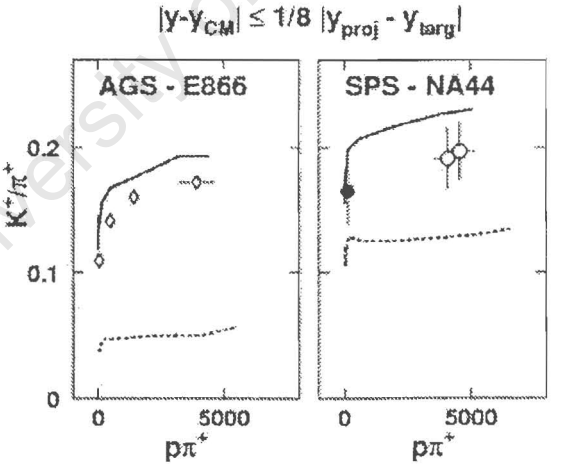

Figure 1.15: Comparison of mid-rapidity K^+/π^+ data from symmetric collisions as a function of the product of mid-rapidity π^+ and proton yields, with RQMD predictions, with (dashed line) and without (solid line) re-scattering [40].

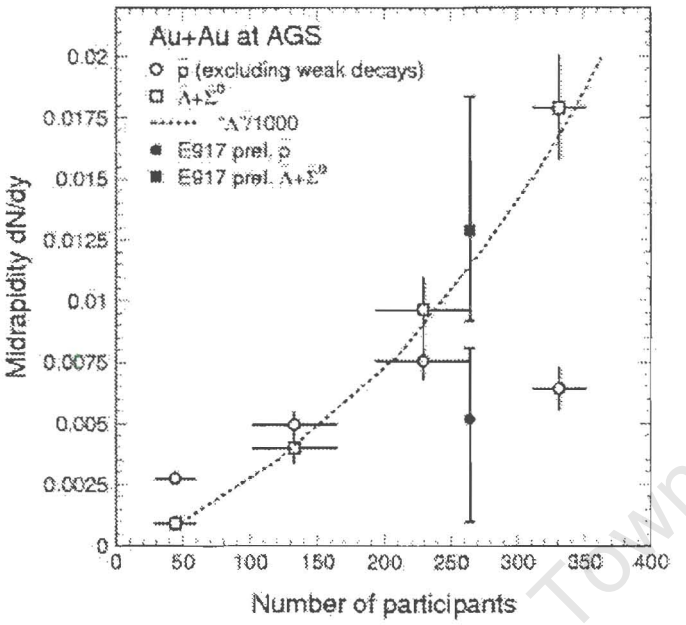

Figure 1.16: Predicted strange antibaryon yields at mid-rapidity as a function of collision centrality [42].

particle ratios from a statistical model in complete equilibrium.

Strange (Anti)Baryon Enhancement

The production of anti-hyperons $(\overline{\Lambda}, \overline{\Sigma}, \overline{\Xi}, \overline{\Omega})$ is expected to be enhanced, compared to hadron gas expectations, if the plasma phase is reached in the transparent region[9], where quark and anti-quark densities are equal, since anti-hyperon production in hadronic collisions is suppressed by the Schwinger factor [6], due to string tension and the strong colour electric field.

The unexplained enhancement of the $\overline{\Lambda}$ to $\overline{p}$ ratio at mid-rapidity with the number of participants (Figure 1.16), as detected at the AGS [42], raises questions of our understanding of strange anti-baryon production. While the anti-proton yield behaves as expected and increases to a saturation multiplicity value due to the high absorption of anti-baryons in a baryon-rich nuclear medium, the anti-lambda yield is seen to continually increase. A large (> 1) anti-lambda to anti-proton ratio has been measured at CERN NA49 and is reproduced by Rafelski and Letessier [43] by assuming sudden hadronisation from a deconfined phase. Rohrich [44] suggests an enhancement of this ratio

[9]See Appendix A1 for a definition of the transparent region.

as a signal for deconfinement as it is an indication of the $\overline{s}$ to $\overline{u}$ ratio. This ratio should reach unity for a plasma formed with no net baryon number, and could reach higher values in a baryon-rich plasma. However, the same argument holds for all ratios of anti-baryons with n strange quarks to anti-baryons with $n-1$ strange quarks so that, barring other effects, an isolated enhanced anti-lambda to anti-proton ratio should not signal deconfinement. A review of strangeness enhancement is given by Rafelski [45].

The WA97 data shows strange baryon and antibaryon enhancement with increasing number of participant nucleons. This data is analysed in detail in Chapters 2 and 3.

According to Sorge [39], 'It has become clear over the years that strangeness enhancement is not as clearly linked to a QGP as initially thought.' According to Rafelski [46], 'strangeness enhancement is today considered to be directly related to the presence of gluons in QGP.' One can see that the status of signals of QGP formation is itself not in equilibrium.

1.4 Aims of this Thesis

Recent Results from the WA97 (and NA57) Collaboration at CERN SPS – which are described in Chapter 2 – have shown a large enhancement in strange particle multiplicities (normalised to p+Be) with system size at 158 A GeV. Seen as a signal for deconfinement – a phenomenon only expected for large systems, this enhancement has stirred the interest of the heavy ion community, with enhancement of the Ω and $\overline{\Omega}$ particles of the order of 16. The enhancement is seen to increase with the strangeness of the particle, and to saturate for large systems ($\approx$ 50 participants). This behaviour is reminiscent of exact strangeness conservation[10], in the vein of Cleymans [47, 48, 49], Redlich [50, 47, 51], Suhonen [47], Hamieh [50], Tounsi [50], Hagedorn [51], Muronga [48], Marais [49] and others. I will in Chapter 3, due to the small number of strange particles produced, make use of the Mixed Canonical Ensemble - with canonical strangeness conservation, and grand canonical charge and baryon number conservation – to describe the observed enhancement of strange particles.

In particular, I will show that the WA97 data are in full agreement with thermal model predictions, even for the smaller p+Be system. Although equilibrium yields of strange particles are a hypothesised signal for QGP, the ability to describe the p+Be system with equilibrium strangeness yields, when no phase transition is expected, opposes the conclusion that a QGP

[10] explained in more detail in the chapter 3

has been formed. As an aside, the dependence of the strange particle yield predictions as the conservation condition is relaxed to exclude the Ω and $\overline{\Omega}$ particles, and then to include exclusive particles of strangeness ± 1 is investigated, in order to evaluate the accuracy of previous canonical formalisms with partial strangeness conservation.

Other models which describe the observed enhancement will be discussed in Chapter 2.

Chapter 2

CERN WA97

2.1 The Data

The CERN WA97 experiment was designed to study strange and multi-strange hadrons at mid-rapidity in p+Be, p+Pb, and Pb+Pb collisions at 158 A GeV/c, specifically to study the production of strangeness as a function of the collision centrality. This study has been motivated by the assumption that a QGP may only be formed in large systems. Thus, by studying the variation of particle yields with system size (multiplicity), a change in the behaviour of the data, along the lines laid out in Chapter 1, would signal deconfinement. For a complete description of the CERN WA97 experimental set-up (as shown in Fig 2.2), see for example [52, 53]. A Pixel Tracking Chamber (PTC) silicon telescope was used to detect particles in the range of approximately one unit of rapidity centred at mid-rapidity ($-0.5 < y_{\rm cm} < 0.5$, $2.41 < y_{\rm lab} < 3.41$) and medium transverse momentum for most strange particles[1].

The symmetry of the Pb+Pb collisions has been exploited as the detected multiplicities could be reflected about mid-rapidity, as shown in Appendix B. Scintillator petal detectors, covering the pseudorapidity region $1 \leq \eta \leq 2$ behind the target, provided an interaction trigger selecting the most central ($\approx>$ 40% most central) [55] of the Pb+Pb collisions, and two planes of micro-strip multiplicity detectors covered all p_T-values in the pseudorapidity region $2 \leq \eta \leq 3$ and $3 \leq \eta \leq 4$ respectively [55], with a total azimuthal acceptance of about 30% [58]. For the Pb+Pb Collisions, a 158 A GeV Pb^{208} beam was incident on a Pb^{208} target of thickness corresponding to 1% of

[1]The p_T and rapidity acceptance of CERN WA97 for Pb+Pb collisions are shown in Appendix B. The acceptance for p+Be collisions was similar and may be found in Ref. [56, 57].

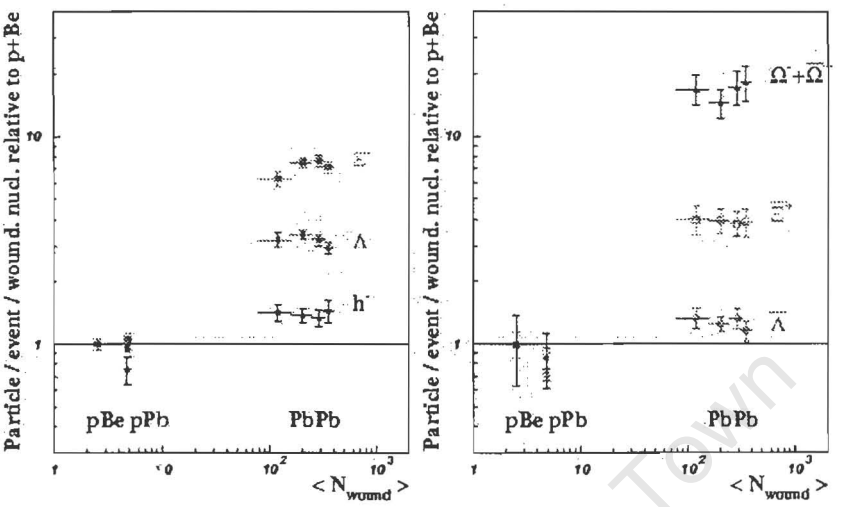

Figure 2.1: The CERN WA97 data - Particle ratios at mid-rapidity per event per wounded nucleon relative to the p+Be yields [62].

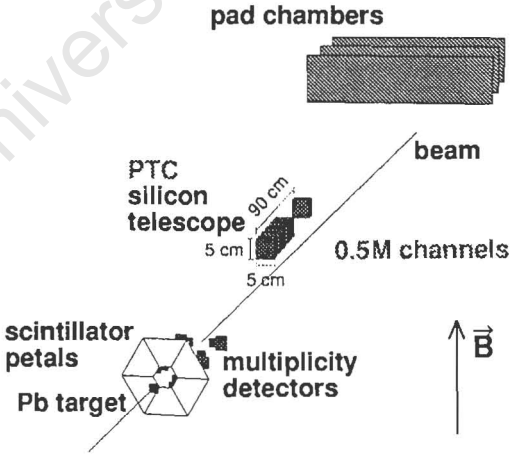

Figure 2.2: WA97 detector set-up [62].

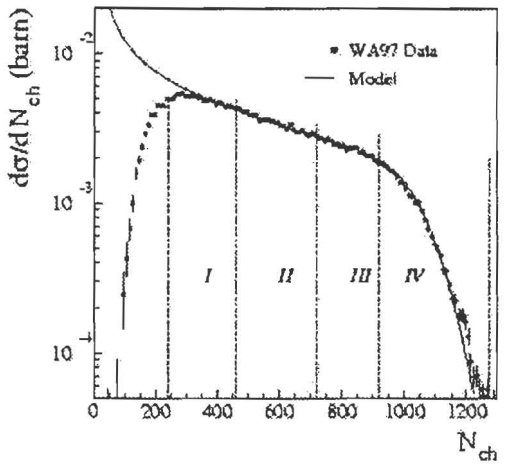

Figure 2.3: Wounded Nucleon Model fit to the multiplicity distribution. The four multiplicity classes used in the data analysis of the Pb+Pb collisions are indicated [58].

the interaction length [55]. Except for the multi-strange particle data[2], the p_T-spectra are consistent with the idea of a thermal system with large-scale transverse flow, as shown in Figure 2.4, and described in Appendix A.4. The centrality of the collision has been determined by calculating the number of wounded nucleons in each collision. According to the wounded nucleon model, the more central an event, the higher the number of wounded nucleons is expected to be [42, 58].

2.1.1 Determination of the Number of Wounded Nucleons

The number of wounded nucleons has been determined within the framework of the Glauber model [42]; a simple model assuming that the projectile nucleons pass through the target nucleus in a straight line with the ability to undergo several collisions with the nucleons of the target [58]. The Glauber model also assumes that the cross section of a projectile and target nucleon colliding is constant and identical to that of a single nucleon (i.e. p+A collisions).

The Wounded Nucleon Model assumes, in addition to the Glauber model, that the average multiplicity in a collision is proportional to the number of nucleons having suffered at least one inelastic collision (the wounded nucle-

[2]Especially the Ω

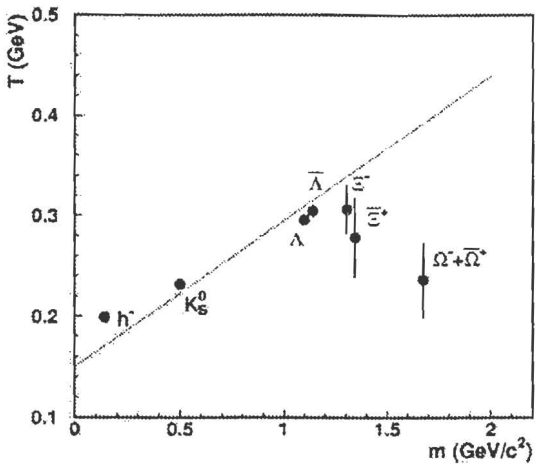

Figure 2.4: Mass dependence of the inverse slopes for the most central Pb+Pb events measured by CERN WA97 [55]. The y-axis corresponds to T_{eff} in Equation A.9.

ons). The only free parameter[3] here is the proportionality constant between the charge particle multiplicity and the number of wounded nucleons [58]. The fit to the inelastic cross-section as a function of the number of charged particles is shown in Figure 2.3. As one can see, the model is accurate for charged particle multiplicities in excess of 300. The four centrality classes for the Pb+Pb collisions have been chosen to include approximately the same number of events.

For the p+A collisions, the minimum bias Glauber model has been used to determine the number of wounded nucleons.

2.1.2 Transverse Mass Spectra

The inverse slopes for singly strange and non-strange particles follow a linear trend, as expected for the case of collective radial flow according to Equation A.9:

$$\frac{d^2N}{dm_T dy} = f(y) m_T \exp^{-m_T/T} \tag{2.1}$$

where the rapidity distribution $f(y)$ is assumed to be a constant plateau in the acceptance region of the experiment. The inverse slope parameters (Figure 2.4 for non-strange and singly-strange particles show evidence for flow,

[3]For other parameters used see [58]

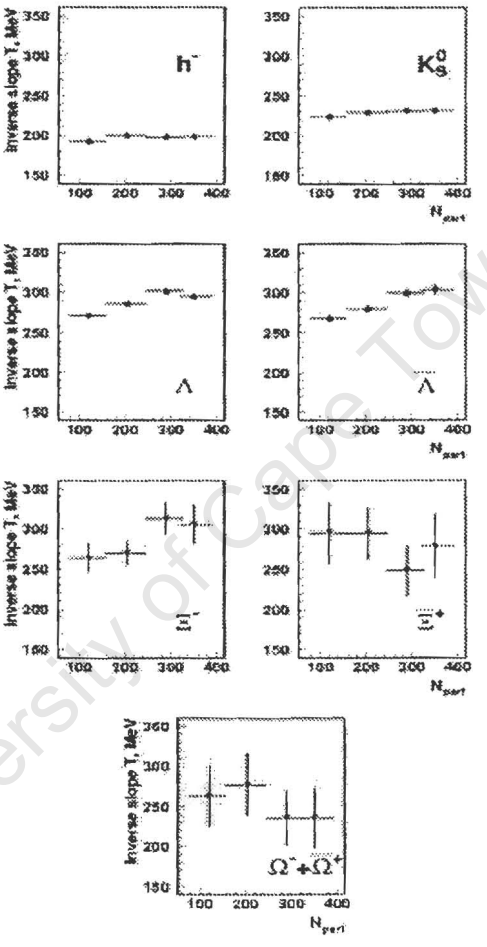

Figure 2.5: Slope parameters for strange particles in 4 centrality bins measured by CERN WA97 [55].

which would boost each particle according to its mass[4]. The T-parameter for the $\overline{\Xi}$ and Ξ particles are, however, very similar, while that of the omega is anomalously low. (The line shown in Figure 2.4 is not a fit, but illustrates the possibility of different behavior of strange and non - strange particles.)

A comparison of the dependence of the T-parameter with centrality in the 4 Pb+Pb centrality bins [55] (as shown below in Figure 2.5), shows that while for multi-strange particles the temperature appears to be constant (although the data has large uncertainty) with variation of the number of wounded nucleons, for the single, and non-strange particles, T increases with centrality. This increase is more pronounced for the heavier particles.

This data suggests, that for the Pb+Pb collisions at CERN WA97, multi-strange baryons decouple early from a system which develops collective radial flow [55]. The variation of the slope parameter with centrality agrees with the picture presented in Equation A.9 of Appendix A.4, as more central collisions are expected to have a larger transverse flow – this affects the heavier particles more than the lighter ones. The properties of the observed m_T-spectra may also be described by assuming a non-constant freeze-out time of the observed particles [60], or according to Ref [61], because the scattering cross sections of the multi-strange baryons in a pion-rich hadron gas are smaller than those of the other particles.

2.1.3 Determination of Particle Multiplicities

The extrapolation of the data to full p_T is done according to the integration of Equation 2.1 [59] where the rapidity distribution $f(y)$ is again assumed to be flat in the acceptance region of the experiment, and T is a free parameter, fixed by the transverse mass slope parameters for each particle.

All strange particles were identified by reconstructing their decays into final states containing only charged particles [55]:

$$K_S{}^0 \rightarrow \pi^+ + \pi^-$$

$$\Lambda \rightarrow p + \pi^-$$

$$\Xi^- \rightarrow \Lambda + \pi^-$$
$$\hookrightarrow p + \pi^-$$

$$\Omega^- \rightarrow \Lambda + K^-$$

[4] as described in Appendix A.4

	p+Be	p+Pb	Pb+Pb			
			Bin1	Bin2	Bin3	Bin4
N_w	2.5	4.75	$120.1^{+5.7}_{-6.1}$	$204.6^{+4.1}_{-4.4}$	$289.0^{+2.5}_{-2.9}$	$350.0^{+0.9}_{-1.1}$
h^-	0.88±0.02	1.26±0.19	60±5	99±8	136±12	178±22
K^0_S		0.098±0.0004	7.7±0.8	14.5±1.1	20.8±1.8	21.9±2.4
Λ	0.0334±0.0005	0.060±0.002	5.1±0.3	9.2±0.4	12.3±0.7	13.7±0.9
$\overline{\Lambda}$	0.0111±0.0002	0.015±0.001	0.71±0.07	1.13±0.09	1.7±0.2	1.8±0.2
Ξ^-	0.0015±0.0001	0.0030±0.0002	0.45±0.03	0.92±0.05	1.32±0.08	1.5±0.1
$\overline{\Xi^+}$	0.00068±0.0001	0.0012±0.0001	0.13±0.02	0.22±0.03	0.30±0.04	0.37±0.06
Ω_T	$(1.6 \pm 0.6) \times 10^{-4}$	$(2.63 \pm 0.78) \times 10^{-4}$	0.13±0.02	0.19±0.03	0.32±0.06	0.41±0.08

Table 2.1: Yields and average number of wounded nucleons measured by the WA97 experiment, where Ω_T is the sum of omega and anti-omega particles [62].

$$\hookrightarrow p + \pi^-$$

The data has not been corrected for feed-down from cascade to lambda particles, as due to the geometry of the experiment the feed-down for weak decays is expected to be of minor importance ($\approx 5 - 10\%$) [57].

Reconstructed strange baryons and anti-baryons have then been corrected for geometrical acceptance and reconstruction efficiency using Monte Carlo simulations accounting for detector efficiencies, background, and electronic noise [57].

2.2 How this Data has been Explained

In the following subsections, I will outline a few other models which have been published to account for the CERN WA97 data. I have not mentioned models which apply only to the Pb+Pb collisions without mentioning the observed enhancement of strange particle production with the number of wounded nucleons. This effect is absent in the range of centrality spanned by the four Pb+Pb centrality classes (Figure 2.1). Likewise, the ability of a particular model to reproduce the rapidity and transverse momentum distributions observed has not been considered unless there has been some attempt at reproducing the multiplicity in all six data bins measured by WA97.

2.2.1 VENUS, RQMD and UrQMD

The majority of what is described below may be found in Ref. [63]. The comparison of the VENUS and RQMD models with experimental data is shown in Figure 2.6.

VENUS (Very Energetic NUclear Scattering): The VENUS model is based on the phenomenological Gribov-Regge Theory (GRT) of hadron – hadron and nucleus – nucleus collisions. A more complete description of the model may be found in [64]. The basic interaction mechanism in this model is the exchange of a Pomeron with well-defined properties, the precise nature of which is not well understood. The Pomeron need not be real. Parameters in the model are tuned to experimentally determined quantities. For example, the string decay and interaction parameters are set to reproduce electron – positron and hadron – hadron data respectively. The model determines the squared amplitudes for inelastic scattering according to which a Monte Carlo simulation generates particles. The interaction of overlapping strings is modelled as quark matter droplet formation.

Relativistic Quantum Molecular Dynamics (RQMD [65]): This model is a semi-classical microscopic approach combining stochastic interactions and classical propogation and is based on the Lund model of hadronic interactions. The basic interaction in this case is based on the string momentum exchange. The strings in this case represent the quarks of the original nucleons. String fragmentation and decay lead to particle production. One of the two decay substrings of the RQMD string decay must be a stable particle, forbidden from further fragmentation. In RQMD, a collection of strings does not fragment independently. They may form ropes, which may be regarded as deconfined quark matter (colour rope formation). Re-scattering interaction probabilities are set from known hadronic cross sections. At large beam energies, the multiple collision scenario follows the paths of the ingoing quarks according to a Glauber type collision series with RQMD, and the additive quark model [66]. Secondaries emerging from fragmenting strings, ropes and resonances may interact with each other, as well as the original ingoing hadrons, via scattering and mean field interactions.

VENUS 4.12 and RQMD 2.3 have been used to simulate the WA97 events. All resonances were allowed to decay, and final-state strange particles stable under strong and electromagnetic decay were measured. GEANT [67] followed the simulated particles through the experimental set-up. The charged

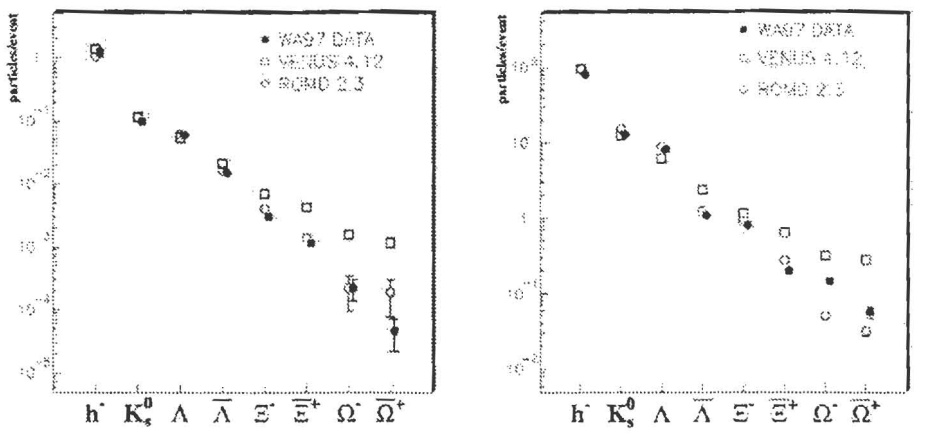

Figure 2.6: Comparison of Venus, and RQMD calculations with CERN WA97 data for p+Pb (left) and the most cental Pb+Pb (right) systems [59].

multiplicity distributions from these models are both accurate until the high multiplicity regions (BIN IV), where they overpredict the charged particle multiplicity.

While both models predict an enhancement of the number of strange particles with strangeness content of the particle [63] for Pb+Pb collisions with respect to p+Pb collisions, and are reasonably accurate otherwise, both fail to reproduce the magnitude of the enhancement of the omega and anti-omega particles.

Figure 2.6 shows the comparison of these models with the WA97 data. VENUS overpredicts the particle multiplicities of the higher mass particles of both the p+Pb and Pb+Pb collisions. The RQMD model gives good agreement with the p+Pb data, but underpredicts the Pb+Pb data for higher mass particles.

UrQMD

Ultra-relativistic Quantum Molecular Dynamics (UrQMD) [68, 69] is an N-body transport model treating binary elastic and inelastic collisions, many-body resonance and string decays. Experimental hadron cross sections and resonance decay widths are used where available. Otherwise, the additive quark model is used to estimate cross sections. The model includes explicit isospin-projected states with masses up to 2.5 GeV. This model differs from the RQMD model in two major ways. The first is that UrQMD does not include the mechanism of colour rope formation – strings fragment according to the Field-Feynman procedure, independantly, from both ends [69]. The

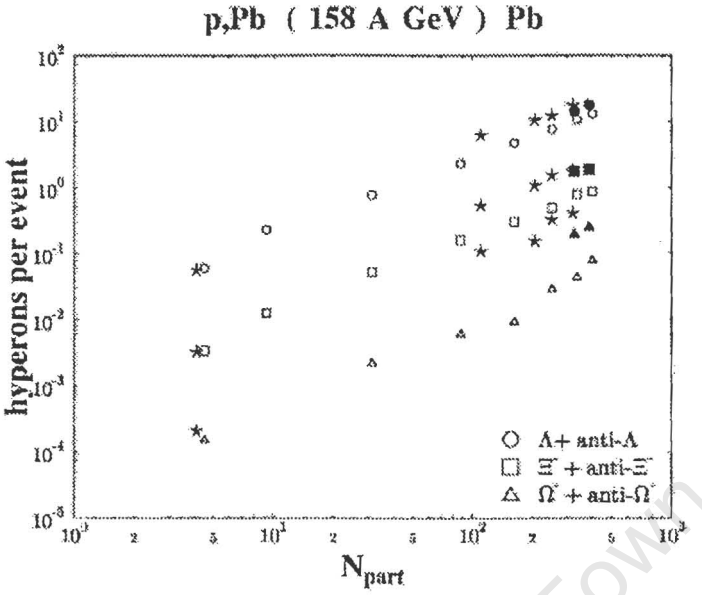

Figure 2.7: Comparison of the UrQMD model with the CERN WA97 data [68]. Stars indicate the data, while shaded symbols represent UrQMD calculations with an increased string tension.

second difference is that while, in RQMD, the time-orderring of collisions may not be frame independant, UrQMD minizes this effect by the choice of collision criterion [69].

The UrQMD model predictions are shown in Figure 2.7. We see that with an increased string tension, the agreement of the model with experimental data is good. The increased tension is analogous to the reduction of quark masses, as expected if deconfinement is achieved.

2.2.2 String Fusion Model

The String Fusion Model [70] is a Monte Carlo simulation based on the Quark Gluon string model and assumes that strings fuse when their transverse positions come within a certain interaction distance. Collisions are assumed to be between two clouds of partons – where the parton – parton interaction leads to the creation of two colour strings. The partons are allowed to interact several times, with the quantum numbers of the fused strings determined by that of the interacting partons, and the energy-momentum of a string being the sum of that of its ancestor strings. Fused strings show an increased string tension giving rise to heavy flavour in the breaking of these strings. Although fusion may take place between multiple strings, Ref. [70] considers only the

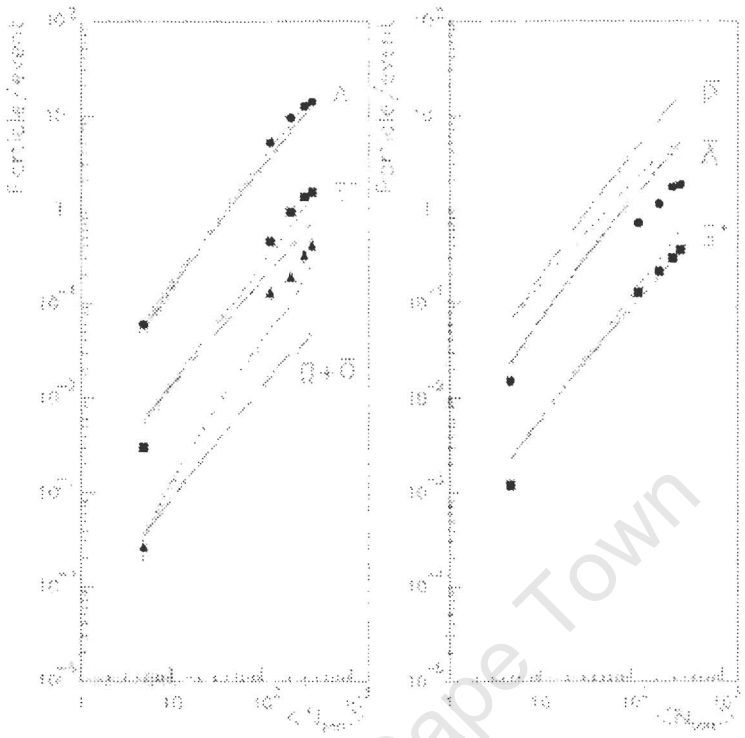

Figure 2.8: Comparison of the String Fusion Model with CERN WA97 data [70]. Dashed lines include re-scattering.

fusion of two strings. The authors have accounted for this by increasing the fusion cross section of the two strings. The model used also accounts for mini-jet production and re-scattering of secondaries. The comparison of the model with CERN WA97 is shown below in Figure 2.8. When including fusion and re-scattering, the data are well reproduced, with the exception of the anti-lambda and omega particles. The model overpredicts particle yields for small systems.

2.2.3 String Fragmentation (LUCIAE)

LUCIAE [71] is a Monte Carlo event generator based on the FRITIOF [72] string model of inelastic hadron – hadron collisions, with the addition of final state interactions. A hadron is assumed to behave as a massless relativistic string, and a hadron – hadron collision may be seen as the multi-scattering of the partons of the colliding hadrons. To describe hadron – nucleus and nucleus – nucleus collisions, a superposition of binary hadron – hadron collisions is considered. The string – string collective interaction is accounted for

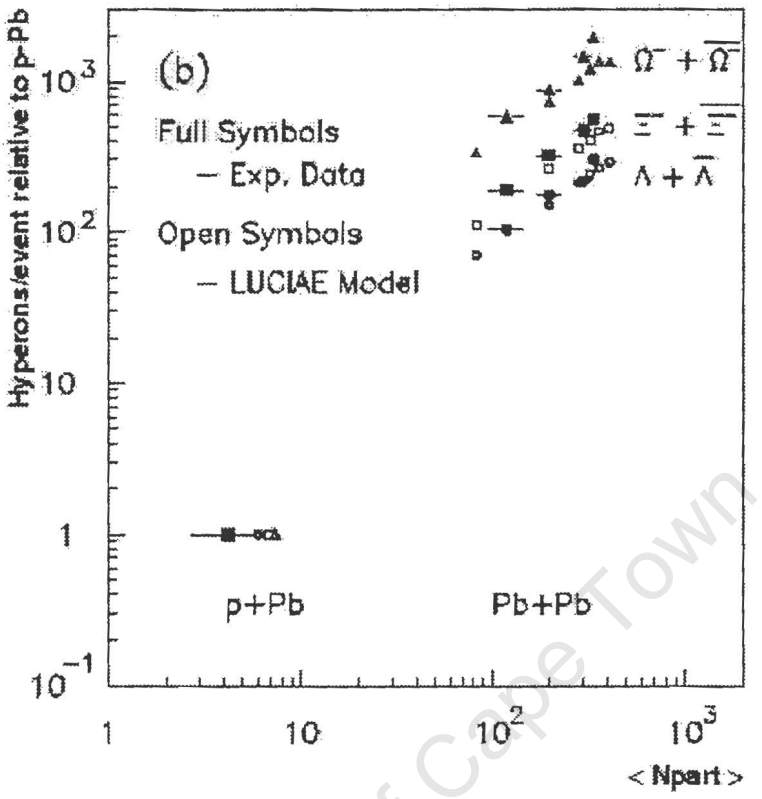

Figure 2.9: LUCIAE simulation predictions, compared to CERN WA97 data [71].

by assuming that several strings produced will interact in a collective way within a cluster, according to the Firecracker model [73]. The production of mini-jets (gluons) in an $h + h$ collision will increase the effective string tension, enhancing the production of strange quark pairs in the string fragmentation region. The enhancement is due to the existence of gluons on the string which give it a fractal structure leading to a higher energy density, which in turn increases the string tension. The agreement of the LUCIAE model with the data is shown in Figure 2.9. The LUCIAE model reproduces the behaviour of the CERN WA97 data. The model slightly underpredicts the yield of multi-strange particles in more central collisions – with the magnitude of the underprediction proportional to the strangeness of the particle.

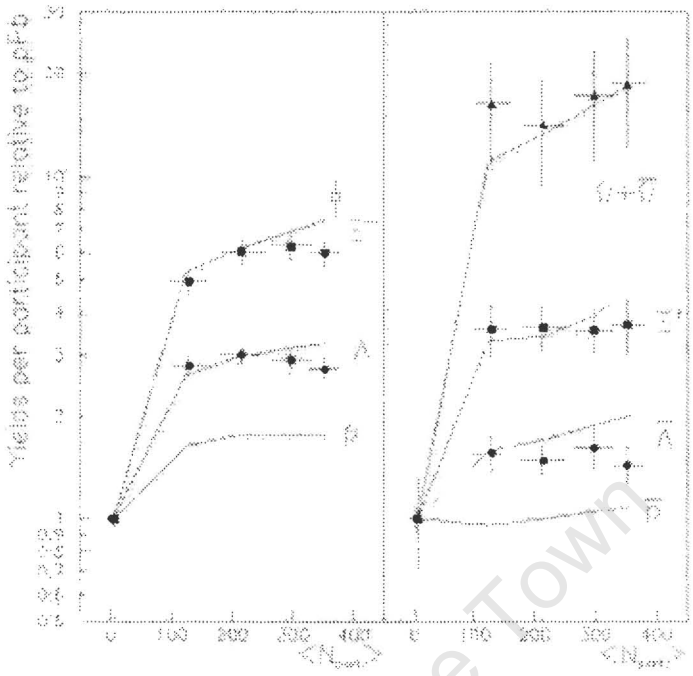

Figure 2.10: Comparison of the Improved Dual Parton Model and CERN WA97 data [74].

2.2.4 Improved Dual Parton Model

The Improved Dual Parton Model [74] is based on the dissociation of the pp cross-section into diquark breaking, and diquark preserving pieces, in order to enhance the increased stopping present in heavy ion collisions compared to pp collisions. The diquark breaking interactions are seen to be responsible for most of the baryon stopping in a heavy ion collision. The increased baryon stopping is proposed as the reason for increased strangeness production seen at CERN WA97. The agreement with experimental data is shown in Figure 2.10. In this model it is evident that the enhancement has not reached saturation. At high $< N_{part} >$ the model is only able to describe the omega yields.

A description of the Dual Parton Model may be found in [75].

2.2.5 HIJING $B\overline{B}$

The HIJING $B\overline{B}$ [76] model extends the valence baryon junction exchange mechanism [77, 78] by including junction – anti-junction loops. In a highly

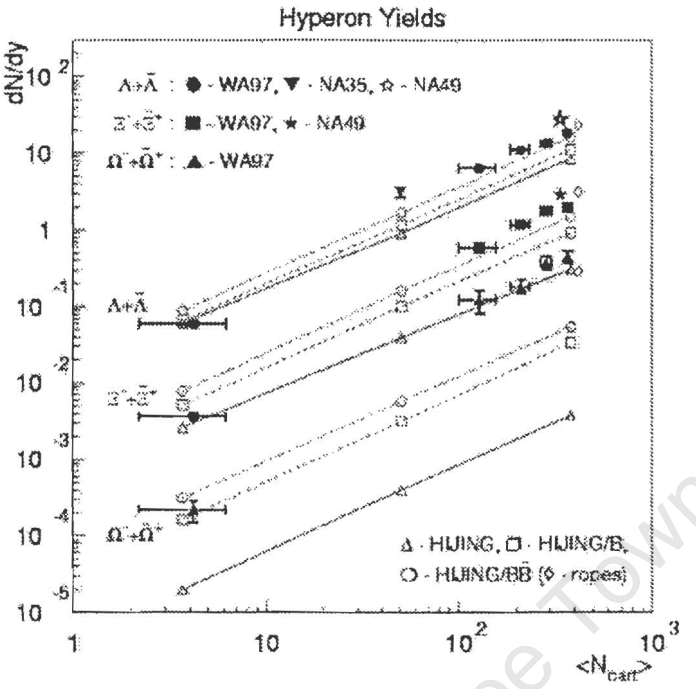

Figure 2.11: HIJING BB predictions compared with CERN WA97 data [76].

excited state, the junction – anti-junction three string configuration fragments to enhance the strangeness content of bayons and anti-baryons. The comparison with experimental data is shown in Figure 2.11. The model still underpredicts the yields of omega and anti-omega particles. It is important to note that the model as implemented does not include final state interactions, and is more accurate than its predecessors (HIJING, and HIJING B).

2.2.6 Thermal Models

An implementation of the mixed canonical formalism[5] with grand canonical conservation of charge and baryon number, and canonical conservation of strangeness, has been investigated by Hamieh et al. [50], and Keränen and Becattini [79]. These models have reproduced the observed enhancement of strange particle yields with number of wounded nucleons, with the degree of enhancement increasing with the strangeness of the particle, and reaching saturation at some stage. Hamieh et al. [50] assume that in addition to the normal volume parameter, which describes the system size at freeze-out, an

[5]A description of the thermal model is given in the next chapter

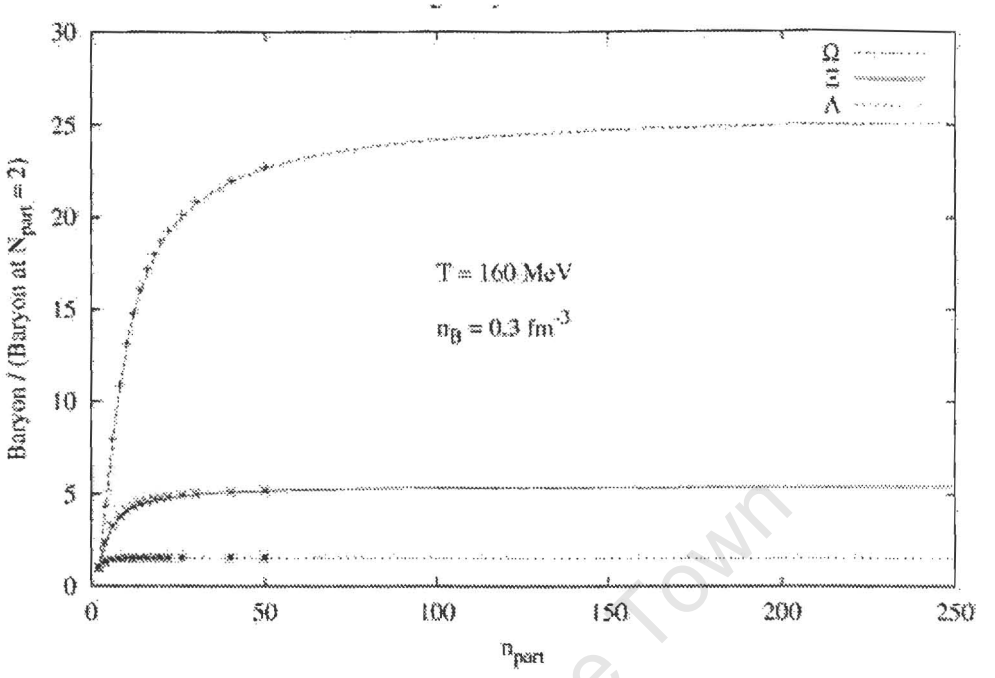

Figure 2.12: Strange particle yields with increasing number of participating nucleons by Becattini, and Keränen [79].

interaction volume is required, which is involved in controlling the particle densities of the strange particles. The effect of this interaction volume is analogous to a strangeness suppression factor (γ) in other thermal models, and is proportional to the number of wounded nucleons in the projectile. This assumption is used to describe the p+Pb data and will be described in detail in Chapter 3. The application by Keränen and Becattini [79] merely reproduces the observed behaviour of the data as seen in Figure 2.12 - no fit has been presented.

The analysis by Hamieh et al. assumes a constant freeze-out temperature for all bins, and μ_B = 150 MeV for the p+Be system and 266 MeV for the Pb+Pb system. The radius of the system is assumed to be of the form $R \sim 1.2(A_{part}/2)^{1/3}$. The variation of particle multiplicities with system size at fixed T and μ_B from this analysis are shown in Figure 2.13, normalised to a system of radius 1.2 fm/c. The ability of this model to reproduce the Pb-Pb data is shown in Figure 2.14.

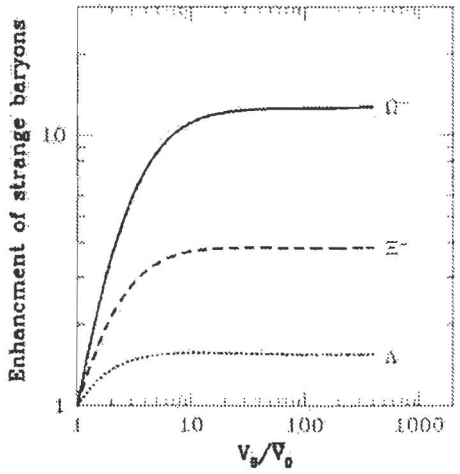

Figure 2.13: Strange particle yields normalised to p+Be predicted by the thermal model with canonical strangeness enhancement [50].

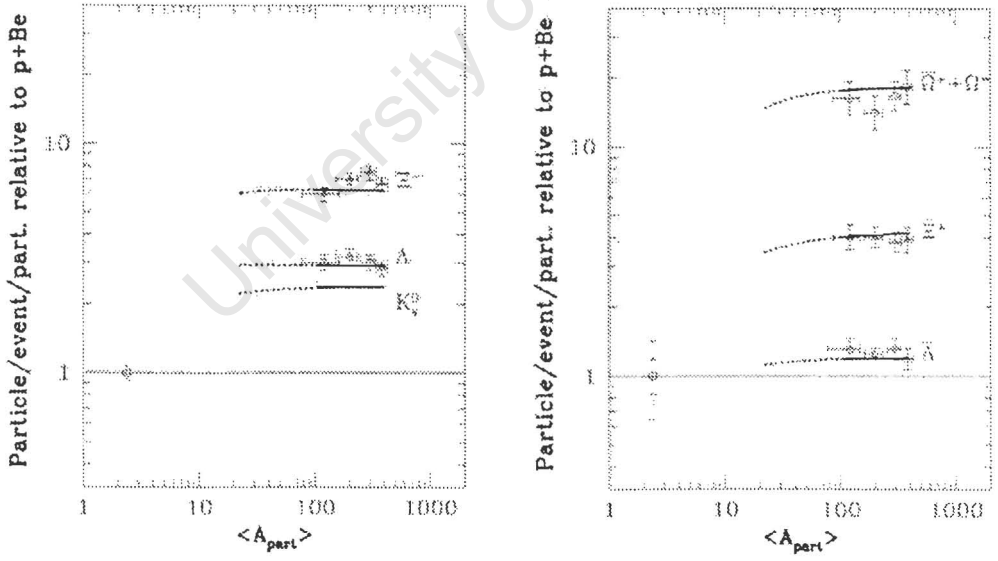

Figure 2.14: Comparison of the thermal model with Pb+Pb data from CERN WA97 [50].

2.2.7 A Comment on these Models

Of the non-thermal models considered here, the LUCIAE and UrQMD models best reproduce the WA97 data across all bins. In the comparison with the data, these models consider the sum of the particle and anti-particle yields for strange particles. These sums are not very sensitive to the anti-baryon yields which are often only 10% of the corresponding baryon yield. All models fail to reproduce the $\Omega + \overline{\Omega}$ yields in central Pb+Pb collisions with the exception of the Improved Dual Parton Model, and the thermal model.

The thermal model with canonical strangeness suppression is shown to qualitatively reproduce the data across all bins, and quantitatively reproduce the data in the Pb+Pb bins. A quantitative thermal fit to the data in all bins is presented in Chapter 3, along with a comparison of the parameters fixed by the thermal model of Hamieh et al. and the one to be presented in this thesis.

It will be shown that the canonical thermal model is able to account for the WA97 data in its entirety.

Chapter 3

A Mixed Canonical Ensemble

3.1 Theoretical Formalism

In order to describe the yields of particles from high energy collisions, the hadron gas model assumes that at the time at which the system breaks up it may be described by statistical thermodynamics. The system is modeled as a gas of hadrons in thermal equilibrium (full occupancy of the available phase space) and may be described by a relatively small number of parameters (T,V,μ). As discussed in Chapter 1, the ability of strange particles to reach equilibrium values of occupancy if the system had not, at some time earlier than τ_{ch}[1], been in the deconfined QGP phase, has been questioned. The system formed in a collision has associated with it certain properties, or rather quantum numbers, which need to be conserved. Where there are a large number of particles concerned, the quantum numbers carried by these particles need only be conserved on average for the system, as a small fluctuation of a large number may be disregarded. As the total number of particles in the system carrying a certain quantum number becomes smaller, it becomes more important to conserve this quantum number exactly.

Within statistical thermodynamics there are three possible formalisms which may be utilised to conserve quantum numbers either exactly, or on average. These are listed below:

Microcanonical Ensemble: In this case all conserved quantities are fixed exactly, and there is a well defined energy.

Canonical Ensemble: This ensemble describes a system at a fixed temperature. The average energy of the system is defined, but the exact energy of the system may fluctuate (a system in a 'heat bath'). All

[1] Thermal Freeze-out time – see chapter 1

conserved properties of the system are conserved exactly, except for the energy.

Grand Canonical Ensemble: The average values of all conserved properties of the system are fixed, although fluctuations are possible. These fluctuations will be of the order $\frac{1}{\sqrt{N}}$ where N is the number of particles carrying the conserved quantity. For large values of N these fluctuations are negligible.

In order to conserve certain quantities exactly, and some on average, a mixed canonical ensemble is required. This marriage of the canonical and grand canonical formalisms is discussed in detail below. In this case, the quantum number strangeness is conserved canonically (exactly). This is motivated by the small number of strange particles observed by CERN WA97. In addition, as has been mentioned previously, the behaviour of the CERN WA97 data is consistent with the transition from a canonical to a grand canonical description – in particular, the increase of the strange particle yields per unit volume with volume until saturation is reached. Baryon number and charge may be conserved on average in the particular case of the CERN WA97 data, as there are large numbers of baryons and charged particles formed. It should be apparent that for large particle numbers, the canonical and grand canonical formalisms agree. Since the canonical ensemble [49] is computationally intensive, until recently such an analysis has not been possible for large systems [79]. This leads to the more frequent use of the grand canonical ensemble, which is justified in most cases. The particle number expressions for Boltzmann and quantum statistics are shown below for the grand canonical formalism, conserving initially particle number, and later baryon number, charge, and strangeness. Following this, the idea of exact strangeness conservation is introduced for the case of Boltzmann statistics.

3.1.1 Grand Canonical Formalism

The most important expression when considering a statistical formalism is the partition function[2](Z). In the case of quantum statistics, the logarithm of the grand canonical partition function, for a gas of particles of mass m, is given by the well-known results:

[2]The sum over all microscopic states from which the macroscopic variables may be derived

$$\ln Z_{BE} = gV \int \frac{d^3p}{(2\pi)^3} \ln \left(\frac{1}{1 - e^{-\frac{\left(\sqrt{m^2+p^2}-\mu\right)}{T}}} \right) \tag{3.1}$$

$$\ln Z_{FD} = gV \int \frac{d^3p}{(2\pi)^3} \ln \left(1 + e^{-\frac{\left(\sqrt{m^2+p^2}-\mu\right)}{T}} \right) \tag{3.2}$$

Z_{BE} (Z_{FD}) is the partition function for bosons (fermions). The particle number expressions $< N >$ may be derived by differentiating Z with respect to μ, dividing the result by Z, and then multiplying by T[3], or more simply, taking the derivative with respect to μ of $\ln Z$ and multiplying by T. This leads to:

$$< N >= gV \int \frac{d^3p}{(2\pi)^3} f(x,p) \tag{3.3}$$

with the distribution function $f(x,p)$ given below:

$$f_Q(x,p) = \frac{1}{e^{\frac{\left(\sqrt{m^2+p^2}-\mu\right)}{T}} \pm 1} \tag{3.4}$$

$$f_B(x,p) = e^{-\frac{\sqrt{m^2+p^2}-\mu}{T}} \tag{3.5}$$

where the upper (lower) sign of $f(x,p)_Q$ corresponds to fermions (bosons) and $f(x,p)_B$ is the Boltzmann distribution function.

The Fermi-Dirac and Bose-Einstein distribution functions may be expanded using:

$$\frac{1}{1-x} = \sum_{n=0}^{\infty} x^n \tag{3.6}$$

As shown below, the first term in the expansion is the Boltzmann distribution function[4].

$$f_Q(x,p) = \frac{1}{e^{\frac{(E-\mu)}{T}} \pm 1} \tag{3.7}$$

$$= e^{-\frac{(E-\mu)}{T}} \times \frac{1}{1 \pm e^{-\frac{(E-\mu)}{T}}} \tag{3.8}$$

[3] Dividing by the co-efficient of μ

[4] where $E = \sqrt{m^2 + p^2}$

$$= e^{-\frac{(E-\mu)}{T}} \times \sum_{k=0}^{\infty} (\mp 1)^k e^{-\frac{(E-\mu)k}{T}} \tag{3.9}$$

$$= \sum_{k=1}^{\infty} (\mp 1)^{k+1} e^{-\frac{(E-\mu)k}{T}} \tag{3.10}$$

For a gas composed of multiple particle species (A), the total partition function is given by the product of the partition functions for each particle species, with a unique chemical potential (μ_A) for each particle type. $< N_A >$ will again be determined by differentiating ln Z by μ_A and multiplying by T.

In a system formed as a result of a heavy ion collision, the number of particles of a particular type is not independently constrained. What must be constrained are the values of the baryon number (B), strangeness (S) and charge (Q) for the entire system. This change affects μ, which now becomes a function of these properties of the particle concerned:

$$\mu_A \rightarrow B_A \mu_B + Q_A \mu_Q + S_A \mu_S \tag{3.11}$$

where μ_A is the chemical potential for a particle of strangeness S_A, baryon number B_A, and charge Q_A. The factors μ_B – the baryon chemical potential, μ_Q – the charge chemical potential, and μ_S – the strangeness chemical potential, are constant for the entire system, and their values constrain these properties of the system as μ previously constrained particle numbers. It is convenient at this time to define the Boltzmann particle number expression[5] for a particle of species A with mass m_A as the one particle partition function for particle A:

$$\ln Z_p = < N_p > = gV \int \frac{d^3p}{(2\pi)^3} e^{-\frac{\sqrt{{m_A}^2+p^2}-\mu_A}{T}} \tag{3.12}$$

This expression will be of use in the next section. In order to account for the expected non-equilibrium strange particle yields, a strangeness suppression factor $\gamma_S \geq 0$ may be introduced. Its value at thermal equilibrium is 1, while $\gamma_S < 1$ ($\gamma_S > 1$) leads to strange particle yields smaller (larger) than the predicted equilibrium values. The factor γ_S was heuristically introduced by Rafelski et al. [80], and formalised by C. Slotta et al. [81]. The distribution functions for a particle of species A with mass m_A, strangeness S_A, baryon number B_A, and charge Q_A, may be expressed as:

[5] which is also the logarithm of the Boltzmann partition function

$$f_Q(x,p) = \frac{1}{\gamma_S^{|S_A|} e^{\frac{\left(\sqrt{{m_A}^2+p^2}-B_A\mu_B-Q_A\mu_Q-S_A\mu_S\right)}{T}} \pm 1} \tag{3.13}$$

$$f_B(x,p) = \gamma_S^{|S_A|} e^{-\frac{\sqrt{{m_A}^2+p^2}-B_A\mu_B-Q_A\mu_Q-S_A\mu_S}{T}} \tag{3.14}$$

where $|S_A|$ is the sum of the valence strange quarks and anti-quarks of particle A.

3.1.2 Exact Strangeness Conservation

The formalism to exactly conserve the strangeness of a system to zero, is developed below using Boltzmann statistics. The accuracy of the Boltzmann formalism is investigated later in this chapter. For this derivation, I will assume that strange particle yields reach equilibrium values and therefore $\gamma_S = 1$. If this condition does not impede the ability of the model to reproduce the data accurately[6], the deviation of strange particle yields from equilibrium values will not be considered.

The Partition Function

The partition function for a system with $S = 0$ may be written as:

$$Z = \delta_{\left(\sum_A \sum_{{n_A}^j} S_A {n_A}^j, 0\right)} \prod_A \prod_j \sum_{{n_A}^j=0}^{\infty} \frac{1}{{n_A}^j!} e^{-\frac{({\epsilon_A}^j - B_A\mu_B - Q_A\mu_Q){n_A}^j}{T}} \tag{3.15}$$

Where ${\epsilon_p}^j$ is the j-th eigenvalue of the energy of a particle of type p. There is no μ_S as strangeness is conserved by the Kronecker δ. As the Kronecker δ only affects strange particles, the partition- and distribution functions for non-strange particles are not affected and are still described by the grand canonical formalism previously mentioned. At this point I will make use of the integral form of the Kronecker δ:

$$\delta_{a,b} = \frac{1}{2\pi} \int_0^{2\pi} d\phi \; e^{i\phi(a-b)} \tag{3.16}$$

The partition function then becomes:

[6] and we shall see that it does not

$$Z = \frac{1}{2\pi}\int_0^{2\pi} d\phi \prod_A \prod_j \sum_{n_A{}^j=0}^{\infty} \frac{1}{n_A{}^j!} e^{-\frac{(\epsilon_A{}^j - B_A\mu_B - Q_A\mu_Q - iS_A\phi)n_A{}^j}{T}} \tag{3.17}$$

Making use of:

$$e^x = \sum_{n=0}^{\infty} \frac{x^n}{n!} \tag{3.18}$$

and replacing the sum over j by integrals over position and momentum:

$$Z = \frac{1}{2\pi}\int_0^{2\pi} d\phi \exp\left(\sum_A \sum_j e^{-\frac{(\epsilon_A{}^j - B_A\mu_B - Q_A\mu_Q - iS_A\phi)}{T}}\right) \tag{3.19}$$

$$= \frac{1}{2\pi}\int_0^{2\pi} d\phi \exp\left(\sum_A V \int \frac{d^3p}{(2\pi)^3} e^{-\frac{\sqrt{m_A{}^2+p^2} - B_A\mu_B - Q_A\mu_Q - iS_A\phi}{T}}\right) \tag{3.20}$$

To proceed further I will define:

$$Z_{S_A} = \sum_{A(S=S_A)} V \int \frac{d^3p}{(2\pi)^3} e^{-\frac{\sqrt{m_A{}^2+p^2} - B_A\mu_B - Q_A\mu_Q}{T}} \tag{3.21}$$

The sum over A now only runs over particles with strangeness S_A. Each term in the sum is the one particle partition function (Equation 3.12) for particle A[7]. The partition function may now be written as:

$$Z = Z_0 \frac{1}{2\pi}\int_0^{2\pi} d\phi \exp\left(\sum_{S_A=1}^{3} \left(Z_{S_A} e^{iS_A\phi} + Z_{-S_A} e^{-iS_A\phi}\right)\right) \tag{3.22}$$

Z_0 is the product of the non-strange particle partition functions. As will soon become apparent, it is useful now to write the partition function as:

$$Z = Z_0 \frac{1}{2\pi}\int_0^{2\pi} d\phi \exp\left(\sum_{S_A=1}^{3} \sqrt{Z_{S_A} Z_{-S_A}} \sqrt{\frac{Z_{S_A}}{Z_{-S_A}}} e^{in\phi} + \sqrt{\frac{Z_{-S_A}}{Z_{S_A}}} e^{-in\phi}\right) \tag{3.23}$$

According to Ref. [82]:

[7] ignoring μ_S as strangeness is being conserved exactly, $\mu_A \to B_A\mu_B + Q_A\mu_Q$

$$e^{\frac{\rho}{2}(t+\frac{1}{t})} = \sum_{m=-\infty}^{m=\infty} I_m(\rho)t^m \tag{3.24}$$

The use of which leads to the expression of Z in terms of three infinite sums of the modified Bessel functions of type I:

$$\begin{aligned} Z &= Z_0 \frac{1}{2\pi}\int_0^{2\pi} d\phi \sum_{p=-\infty}^{p=\infty}\sum_{q=-\infty}^{q=\infty}\sum_{r=-\infty}^{r=\infty} e^{i(r+2q+3p)\phi} I_r(2\sqrt{Z_1 Z_{-1}})\left(\sqrt{\frac{Z_1}{Z_{-1}}}\right)^r \\ &\times I_q(2\sqrt{Z_2 Z_{-2}})\left(\sqrt{\frac{Z_2}{Z_{-2}}}\right)^q I_p(2\sqrt{Z_3 Z_{-3}})\left(\sqrt{\frac{Z_3}{Z_{-3}}}\right)^p \end{aligned} \tag{3.25}$$

Completing the integration over ϕ enforces the condition $r+2q+3p=0$ or rather, $r=-2q-3p$, so finally one may write:

$$\begin{aligned} Z &= Z_0 \sum_{p=-\infty}^{\infty}\sum_{q=-\infty}^{\infty} I_{-2q-3p}(2\sqrt{Z_1 Z_{-1}})\left(\sqrt{\frac{Z_1}{Z_{-1}}}\right)^{-2q-3p} I_q(2\sqrt{Z_2 Z_{-2}}) \\ &\times \left(\sqrt{\frac{Z_2}{Z_{-2}}}\right)^q I_p(2\sqrt{Z_3 Z_{-3}})\left(\sqrt{\frac{Z_3}{Z_{-3}}}\right)^p \end{aligned} \tag{3.26}$$

Particle Number Expressions

The derivation of the particle number expressions is similar to the procedure used earlier where the derivative of the partition function with respect to μ gave the particle numbers. In this case, a parameter $\lambda_p = e^{\mu_p}$ is introduced. To determine for example, the number of particles of type A formed, the one particle partition function term for particle A ($\ln Z_A$ defined by Equation 3.12) in Z is multiplied by λ_A. The derivative of the total partition function with respect to λ_A is then evaluated at $\lambda_A = 1$, and divided by the partition function. The particle number expressions for strange particles are shown below. There is no need to multiply by T as μ_A has no coefficients.

For a particle of species A, the number of particles present at equilibrium in a thermal system is given by

$$< N_A >= \frac{Z_0}{Z}\frac{1}{2\pi}\int_0^{2\pi} d\phi\ (\ln\ Z_A)\ e^{iS_A\phi}\ \exp\left(\sum_{S_p=1}^{3}\left(Z_{S_p}e^{iS_p\phi} + Z_{-S_p}e^{-iS_p\phi}\right)\right) \tag{3.27}$$

The transformation to Bessel functions is still possible and now leads to:

$$< N_A > = \frac{Z_0}{Z} (\ln\ Z_A) \frac{1}{2\pi} \int_0^{2\pi} d\phi \sum_{p=-\infty}^{p=\infty} \sum_{q=-\infty}^{q=\infty} \sum_{r=-\infty}^{r=\infty} e^{j(r+2q+3p+S_A)\phi}$$
$$\times I_r(2\sqrt{Z_1 Z_{-1}}) \left(\sqrt{\frac{Z_1}{Z_{-1}}}\right)^r I_q(2\sqrt{Z_2 Z_{-2}}) \left(\sqrt{\frac{Z_2}{Z_{-2}}}\right)^q$$
$$\times I_p(2\sqrt{Z_3 Z_{-3}}) \left(\sqrt{\frac{Z_3}{Z_{-3}}}\right)^p \qquad (3.28)$$

This time the integral over ϕ leads to the condition $r = -2q - 3p - S_A$. The particle number expression in this case may therefore be expressed as:

$$< N_A > = \frac{Z_0}{Z} (\ln\ Z_A) \sum_{p=-\infty}^{\infty} \sum_{q=-\infty}^{\infty} I_{-2q-3p-S_A}(2\sqrt{Z_1 Z_{-1}}) \left(\sqrt{\frac{Z_1}{Z_{-1}}}\right)^{-2q-3p-S_A}$$
$$\times I_q(2\sqrt{Z_2 Z_{-2}}) \left(\sqrt{\frac{Z_2}{Z_{-2}}}\right)^q I_p(2\sqrt{Z_3 Z_{-3}}) \left(\sqrt{\frac{Z_3}{Z_{-3}}}\right)^p \qquad (3.29)$$

In this expression, ln Z_A appears many times; once as shown explicitly above, and repeatedly within the Bessel functions (in the numerator, and the denominator). When describing the thermal model application by Hamieh et al. [50] in Chapter 2, the introduction of an interaction volume for strange particles was mentioned. Ref. [50] has assumed that ln Z_A explicitly shown above is different to ln Z_A in the Bessel functions by virtue of the volume term (V) in ln Z_A not being the same in these two cases. We see from the above derivation of particle number that, theoretically, these volume terms must agree.

The particle number expression may be rewritten for particles with strangeness equal to one as:

$$< N_A >= C_S\ \ln\ Z_A \qquad (3.30)$$

The reader is reminded that ln Z_A is the grand canonical particle number expression for the case of Boltzmann statistics (used in this derivation). C_S is a measure of the Canonical correction to the grand canonical particle number expression.

3.2 Implementation

In this section we explore if canonical strangeness suppression at small volumes (compared to grand canonical equilibrium particle yields) is able to explain the enhancement of strange particle yields per wounded nucleon from small to large systems, as measured by CERN WA97. Ideally the thermal model would only be implemented where 4π integrated data were available, but as only data that has been measured at mid-rapidity is published, I am forced to fit the ratios of particle yields at mid-rapidity by assuming these ratios are in agreement with the 4π integrated ratios. A theoretical comparison of the mid-rapidity particle number ratios with thermal model 4π integrated ratios has been developed by Cleymans et al. [83]. The ratios are found to agree in the special case of boost-invariant cylindrical expansion of the system. Experimentally, ratios of particle to anti-particle yields[8] at mid-rapidity[9] have been compared to 4π integrated yields and shown to be in agreement for S+S collisions at 200 A GeV by the CERN NA35 collaboration [85]. In addition, and perhaps of greater interest, the 4π integrated ratio $\overline{\Xi}/\Xi$ measured by CERN NA49 for Pb+Pb collisions at 158 A GeV has been shown to agree with the corresponding CERN WA97 mid-rapidity ratio [86].

As the mixed canonical formalism has been derived here for the case of Boltzmann statistics, it is worth noting that the second term in the series expansion of the correct quantum statistical distribution function (Equation 3.10) for kaons gives a correction to the kaon numbers of the order of 3% at a temperature of 150 MeV. The magnitude of the correction increases slightly with temperature and decreases with the mass of the particle concerned. The corrections to the Boltzmann distribution functions due to quantum mechanics are expected to affect the kaons more than any other strange particle, as they are the lightest of the strange particles. With errors of 3% and less, the use of Boltzmann statistics to describe the strange particles is justified. From the equilibrium thermal values of all resonances in the Particle Data Booklet [87] at chemical freeze-out, the model accounts for the decay of resonances according to the branching ratios in [87], and in line with the data, as described in Chapter 2, does not account for feed down. As previously mentioned feed down corrections are expected to be of the order of between five and 10 percent [57]. For all mixed canonical analyses the parameter μ_Q fit to zero, and has been subsequently removed as a free

[8] The reason for checking particle to anti-particle ratios is that the masses of the particles in the ratio are equal - this leads to these particles being equally affected by flow. This in turn minimises the errors of introduced by considering a limited kinematic region [84].

[9] In symmetric collisions the majority of new particles are produced at mid-rapidity.

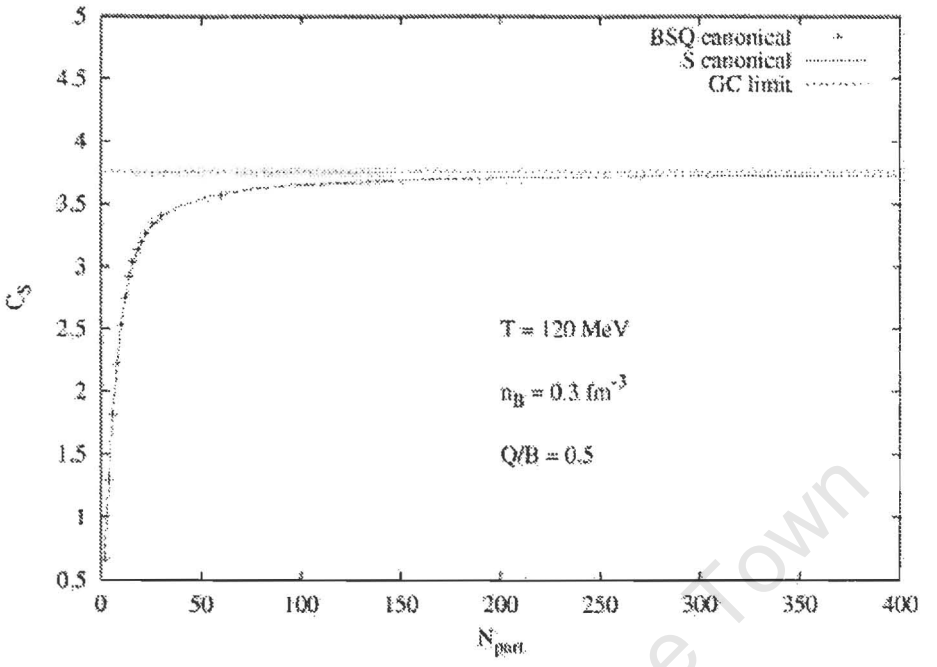

Figure 3.1: C_s - the correction factor to the grand canonical particle number expression, for exact baryon number (B), strangeness (S), and charge (Q) conservation, and exact strangeness conservation (S), for particles of strangeness one [79]. See Equation 3.30 for a definition of C_S.

parameter. For a 4π integrated Pb + Pb system, μ_Q is expected to be small and negative, but at mid-rapidity the approximation $\mu_Q = 0$ is acceptable as the system may show partial nuclear transparency.

The applicability of this model to the small p+Be system may be in doubt, as one may expect that a full canonical treatment as in Ref. [49] is required. This is not so. It has been shown by Becattini and Keränen [79], that a full canonical formalism (i.e. exact baryon number, strangeness, and charge conservation) and a mixed canonical formalism are in exact agreement when predicting particle numbers from heavy ion collisions, as shown in Figure 3.1 using the variable C_S defined in the last chapter.

3.2.1 Analysis A

When fitting the data, it has already been mentioned that particle ratios were used. Unfortunately if I made use of only the particle to anti-particle ratios I would have had only two data points per system. In a model with at

least three free parameters, this is decidedly sub-optimal. The main result of this thesis is based on fitting the ratios of the strange particle yields to the yield of negatives for each case in Table 2.1. The negatives yield is used for each ratio due to its superior statistics. In addition it provides a measure of the entropy of the collision (since pions are the most abundant particle species.) The major contribution to the negatives yield is expected to be from π^- particles. For these bosons, the second term in the expansion of the quantum mechanical distribution function (Equation 3.10) at 150 MeV is of the order of 30% . It is unacceptable to ignore this correction to the Boltzmann approximation when attempting to describe the data. Considering that the non-strange particle yields predicted by the model are independent of the exact conservation of strangeness, the full quantum mechanical particle number expression given by Equations 3.3, and 3.13 is evaluated for all non-strange particles. The parameters obtained in this way are shown in Table 3.1 as Analysis A[10]. The χ^2 for each system is good, and there are three (two) degrees of freedom for the p+Pb, and Pb+Pb systems (p+Be system).

3.2.2 Analysis B

Analysis B has only three data points ($\frac{\overline{\Lambda}}{\Lambda}$, $\frac{\overline{\Xi}}{\Xi}$ and $\frac{\overline{\Xi}}{\Lambda}$) for each fit. The need for a third data point in order to fit the three parameters of the model, necessitated the use of the ratio $\frac{\overline{\Xi}}{\Lambda}$. This analysis has no free parameters, but shows reasonable agreement with Analysis A. The large uncertainties of the fitted parameters are unavoidable. The small values of χ^2 in this analysis are due to the lack of free parameters. Interestingly, fitting these ratios proves impossible for the p+Pb system. The hypothesis of Hamieh et al., [50] of a special 'interaction volume' for strange particles in this system cannot be tested, as the particle ratios would depend only on this interaction volume, as the regular volume cancels in the ratio of the particle multiplicities.

3.2.3 Analysis C

Analysis C determines the grand canonical best fits to the data assuming quantum statistics. In this case, there is no volume dependence of the particle ratios and I have included μ_S and μ_Q. This procedure fails for the p+Be system. As may be expected for systems of this size, a full canonical treatment [49] is required. In this analysis, the parameters fitted for

[10]The table also includes the χ^2 and fit parameters for two other analyses described in detail below

	p+Be	p+Pb	Pb+Pb			
			Bin1	Bin2	Bin3	Bin4
Analysis A Ratios of Strange Particle to Negatives Multiplicities						
χ^2	0.756	1.85	2.07	0.427	1.58	1.45
T	162±4	172±2	161±4	164±4	166±4	159±5
μ_B	111±7	157±39	201±25	230±38	228±28	204±30
R	1.39±0.14	1.16±0.39	6.81±8.73	9.88±10.9	6.78±9.39	10.4±6.8
Analysis B Ratios of Particle Yields to that of their Anti-Particles						
χ^2	$\sim 10^{-6}$	60287	$\sim 10^{-7}$	$\sim 10^{-4}$	$\sim 10^{-3}$	$\sim 10^{-2}$
T	157±25	-	171±17	161±15	153±35	163±45
μ_B	106±31	-	229±55	222±46	190±61	220±30
R	1.50±0.83	-	2.17±2.03	6.06±8.92	9.38±7.12	8.08±6.83
Analysis C Grand Canonical Fit						
χ^2	78	17.5	1.53	0.15	0.70	0.97
T	-	143±8	173±20	165±4	166±5	171±20
μ_B	-	205±106	282±96	227±39	203±45	265±120
μ_Q	-	-109±52	-54±68	0±50	0±60	-62±86
μ_S	-	105±63	110±73	54±25	39±28	94±97

Table 3.1: Parameters obtained for various analyses as described in the text. The temperature (T) and chemical potential (μ_B) are in MeV. The radii (R) are given in fm. If χ^2 is greater than 50, the fit parameters are not shown.

Bin 4 immediately catch the eye – with high uncertainty values even though $\chi^2 < 1$. This is especially puzzling when one notices that this is not the case in Analyses A or B. The T and μ_B parameters agree with those obtained by Becattini et al. [88], for a grand canonical description of the 4π-integrated data for central symmetric Pb^{208} collisions at 158 A GeV by the CERN NA49 collaboration.

3.2.4 Comment on Analyses A, B, and C

The common parameters in Analyses A, B, and C agree within one standard deviation. The ability of this mixed canonical ensemble to describe the small p+Be system is in agreement with the work of Keränen et al. [79], as shown in Figure 3.1, and mentioned at the beginning of this chapter.

3.2.5 Variation of T, R, and μ_B with $< N_{wound} >$

In order to fully reproduce the CERN WA97 data as represented in Figure 2.1, it is necessary to determine a relationship between the parameters μ_B, radius R, and T obtained from the fits of Analysis A and the number of wounded nucleons. The fits used are shown in Figures 3.2, 3.3, and 3.4 as well as the parameters obtained from a full Boltzmann treatment[11]. The parameters obtained from the p+Pb data have not been considered because of their prediction of a volume smaller than that of the p+Be system.

Temperature

As may be seen in Figure 3.2, it appears initially that the temperature increases with centrality. However, the last data point does not fit this hypothesis, and the variation of chemical freeze-out temperature with number of participants has been assumed to be constant ($T = 163$ MeV). This is in agreement with the canonical thermal model fit to the NA49 data by Becattini et al. [88] to central Pb+Pb data. This temperature value is slightly less than that of the mixed canonical model of Hamieh et al. [50] as described in Chapter 2.

Radius

The large uncertainties of the radius parameter means that almost any function may be fitted to the data (Figure 3.3). In order to reproduce the WA97 data, knowledge of the variation of system size with average number of wounded nucleons is required. The function shown in Figure 3.3 is of the form $< N_{wound} >= R^3 + b$ with $b < 0.5$ adjusted to reproduce the WA97 data (Figures 3.6 and 3.5). This differs from the dependence of the Radius on A_{part} assumed by Hamieh et al. [50] where $A_{part} \sim 1.3 - 1.7R^3$.

The large uncertainty in the radius for the larger systems is not surprising, as the ratios being fitted are expected to show a small volume dependence, due only to canonical strangeness suppression. The effects of canonical strangeness suppression decrease with system size as one approaches the grand canonical limit where ratios of particle multiplicities have no volume dependence.

Baryon Chemical Potential

Figure 3.4 shows the variation of the baryon chemical potential with system size. This function increases rapidly before saturating. All the Pb+Pb cen-

[11] using Boltzmann statistics for strange, and non-strange particles

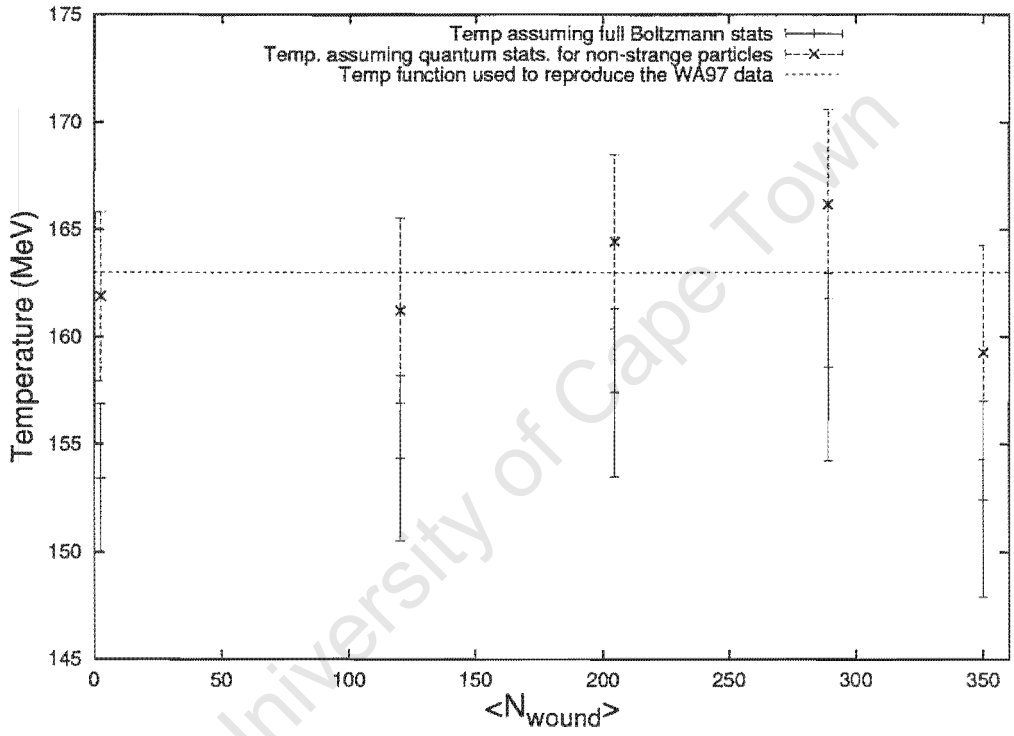

Figure 3.2: Variation of the chemical freeze-out temperature (T) of the system with number of wounded nucleons.

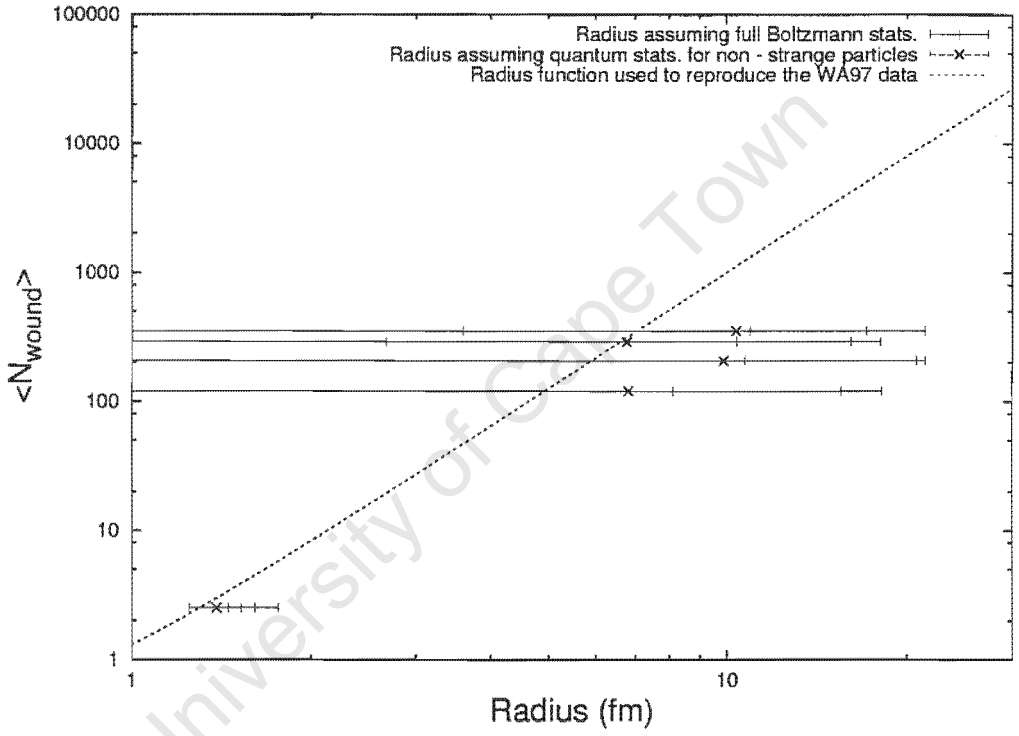

Figure 3.3: Variation of the radius (R) of the system with the number of wounded nucleons.

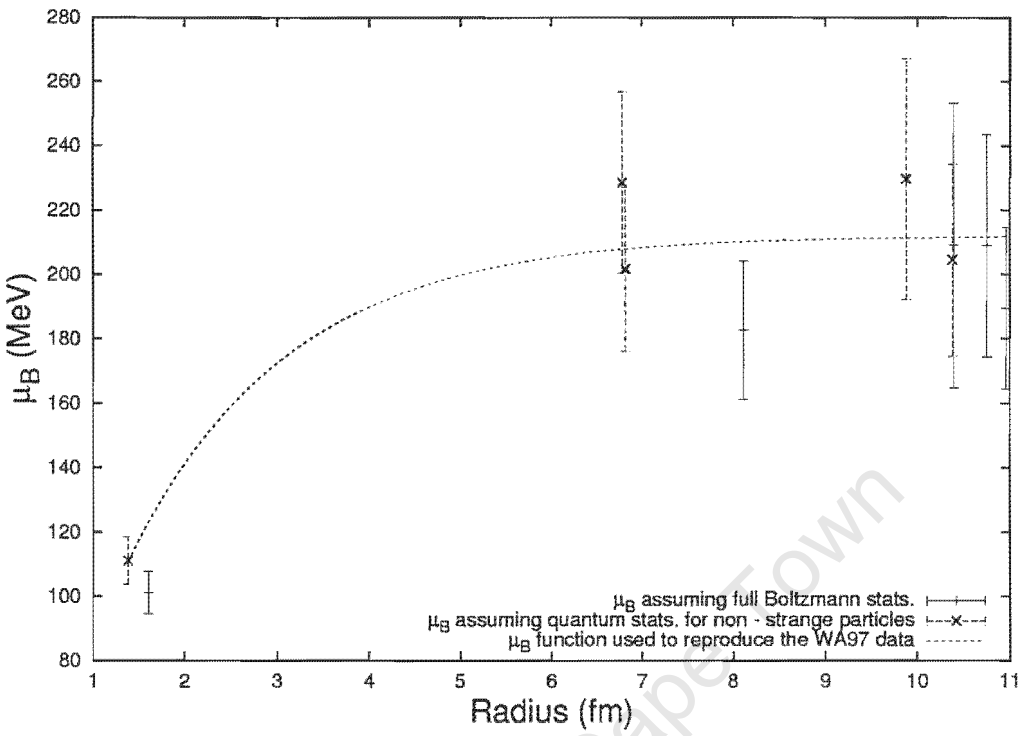

Figure 3.4: Variation of the baryon chemical potential (μ_B) with radius.

trality bins are described by the saturation value of approximately 210 MeV. The obtained values of μ_B in the central Pb+Pb bin are in agreement with that of Becattini et al. [88]. The μ used for the Pb+Pb bins by Hamieh et al. [50] is just outside one standard deviation of the values obtained by this analysis. For the p+Be system the value of μ_B used in Ref. [50] (150 MeV) is much larger than that obtained in this analysis (111 ± 7 MeV) .

The exact variation of μ_B, T and R in the range between the p+Be and Pb+Pb may differ from what is shown here and new data from CERN NA57 in this range are eagerly awaited.

The figures mentioned above (3.2, 3.3, and 3.4) also show the variation of the parameters T, R, and μ_B with centrality in the case where all particle multiplicities are assumed to be Boltzmann. These parameters are seen to be in agreement with the parameters from Analysis A. The χ^2 for the purely Boltzmann fits were of the order of 1 for all systems.

3.2.6 Reproducing Figure 2.1

Figures 3.5 and 3.6 show the ability of the model to reproduce the data (Figure 2.1) using the functions in Figures 3.2, 3.3, and 3.4 to predict the

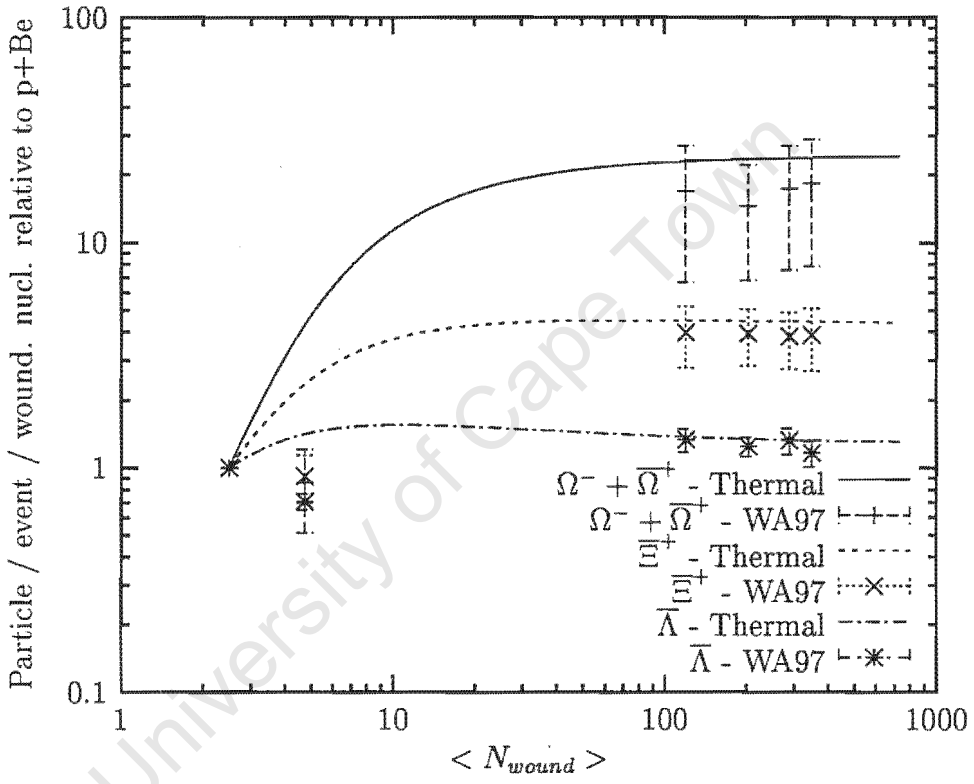

Figure 3.5: Comparison of the hadron gas model with exact strangeness conservation and CERN WA97 data for the Ω and strange anti-particles.

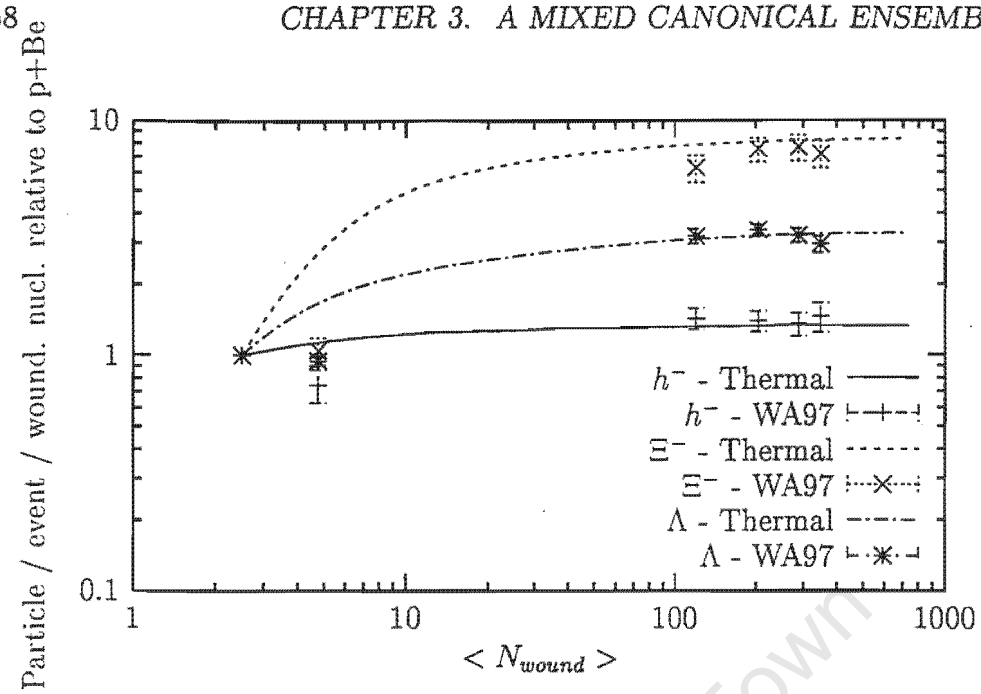

Figure 3.6: Comparison of the hadron gas model with exact strangeness conservation and CERN WA97 data for negatives and strange particles.

variation in chemical freeze-out temperature T, radius R, and baryon chemical potential μ_B with average number of wounded nucleons. As is clear, the agreement of the model with experimental data is good. The exact shape of the thermal model predictions shown in Figure 3.5 and 3.6 show a large dependence on the exact relationship between number of wounded nucleons and system size, and a weaker dependence on the functional fit to the other two parameters. This is rather unfortunate as the thermal model R values obtained have uncertainties equal to their magnitude, so this relationship is not contrained by the model.

3.2.7 Investigation of the Importance of Including All Strange Particles in the Formalism

Previously, there have been many applications of the mixed canonical model with canonical strangeness enhancement where the formalism included only singly-strange, or $|S| \leq 2$ particles. To compare these formalisms to the full canonical strangeness conservation model described here, I attempt to reproduce the WA97 particle behaviour conserving only $|S| \leq 2$, and then $S = \pm 1$ particles[12], letting the T, R, and μ_B parameters vary as shown in

[12]The modification to the model presented in the previous chapter is minimal and all that changes is the number of terms in the sum over S_p in equation 3.22

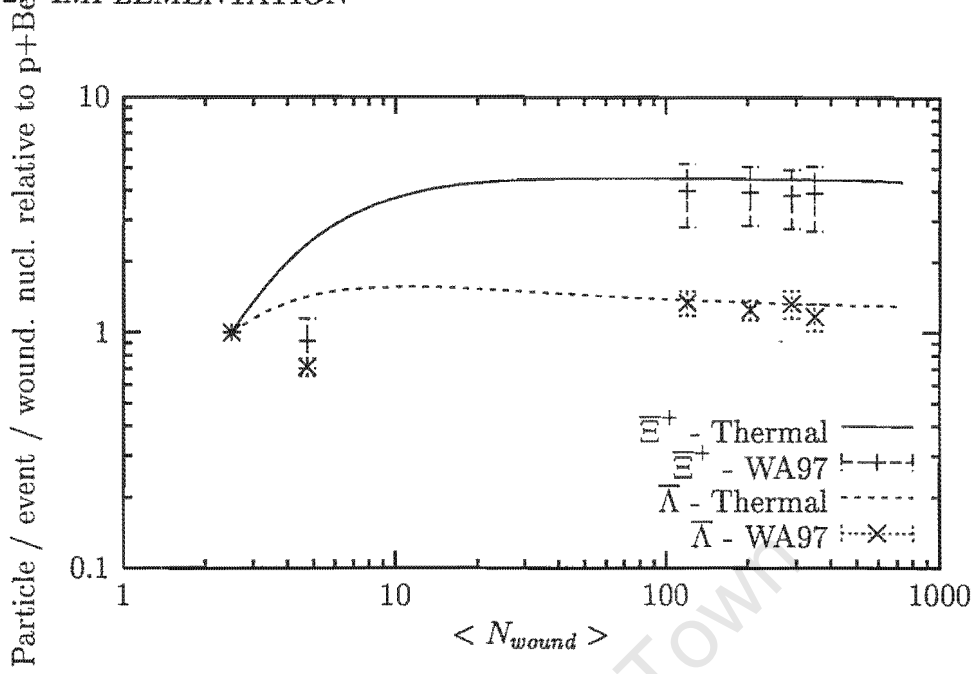

Figure 3.7: Comparison of the hadron gas model with exact strangeness conservation up to doubly strange (anti-)particles with WA97 data for the Ω and strange anti-particles.

Figures 3.2, 3.3, and 3.4.

Figures 3.7 and 3.8 show the model predictions for exact conservation of $|S| \leq 2$ particles. From these figures it is apparent that neglecting the Ω^- and $\overline{\Omega}^+$ in a thermal model with exact strangeness conservation, to describe particle yields of $|S| \leq 2$ particles, is justified.

Figure 3.9 shows the results obtained assuming exact strangeness conservation for only $S = \pm 1$ particles. The thermal model prediction is shown to differ slightly in this case, but this variation is small enough to be ignored.

Figures 3.7, 3.8, and 3.9 show behaviour normalised to p+Be. It is possible that differences in particle multiplicities may cancel in the normalisation to p+Be. The predicted values of the ratios of exactly conserved strange particles to pions in the p+Be system for $|S| \leq 2$ or $S = \pm 1$ conservation are unchanged (until the third significant figure), when using the parameters (T,R, and μ_B) from Analysis A, obtained by conserving ($|S| \leq 3$).

From these results, it is apparent that, in order to describe yields of a particle of strangeness S, a model implementing canonical strangeness conservation need only consider the exact conservation of particles of strangeness $\leq S$.

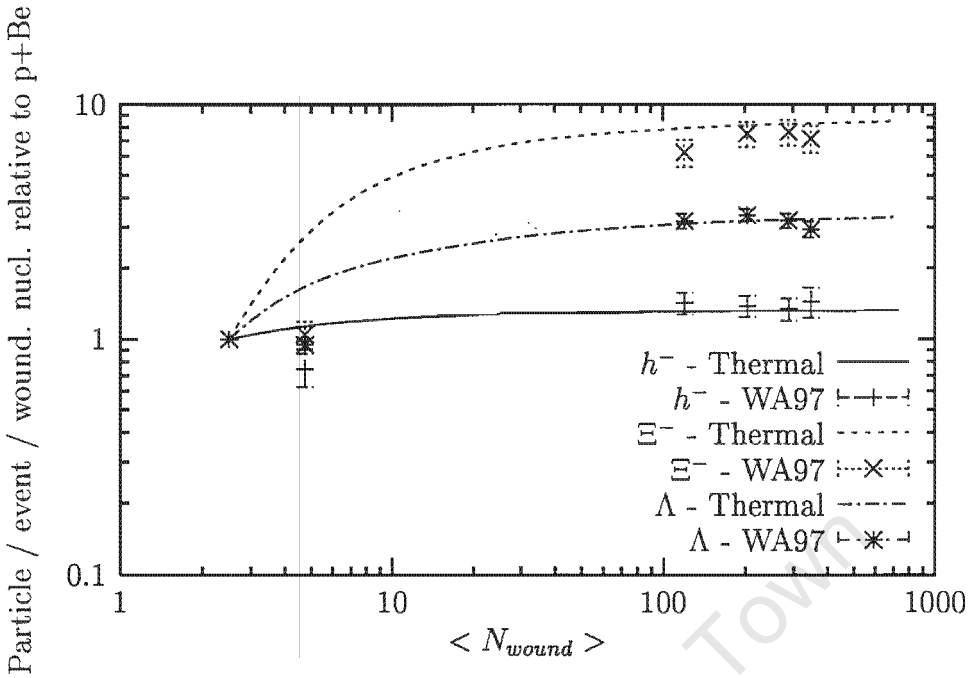

Figure 3.8: Comparison of the hadron gas model with exact strangeness conservation up to doubly strange (anti-)particles with WA97 data for negatives and strange paricles.

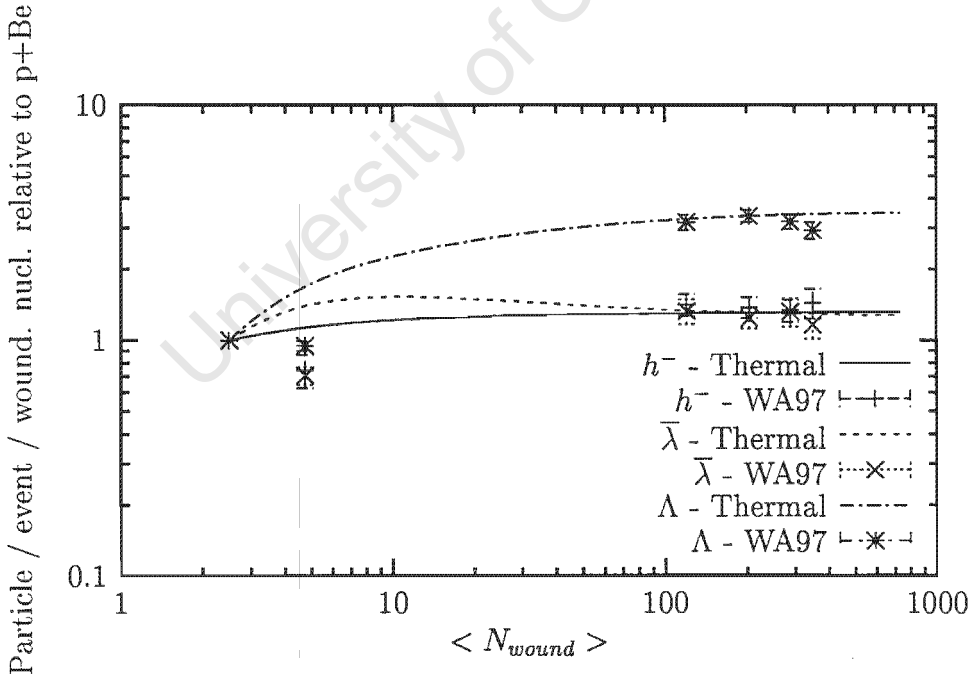

Figure 3.9: Comparison of the hadron gas model with exact strangeness conservation of singly strange (anti-)particles with WA97 data.

3.3 Conclusion

A thermal model conserving baryon number and charge on average, and strangeness exactly has been used to describe particle yields from heavy ion collisions. The formalism includes all strange particles. The model has been applied to the CERN WA97 data (Table 2.1, and Figure 2.1), and is shown to be able to qualitatively, and quantitatively reproduce the data for all centrality classes (Figures 3.5 and 3.6). The accuracy of the model parameters (temperature T, radius R, and baryon chemical potential μ_B) is restricted by the lack of 4π integrated particle yields for multi-strange particles. In order to reproduce Figure 2.1 accurately, some knowledge of the variation of T, R, and μ_B was required. A functional form of the variation of these parameters with the number of wounded nucleons has been determined and is presented in Figures 3.2, 3.3, and 3.4.

The parameters obtained by this model for the central Pb+Pb bins are in agreement with the 4π thermal model application of Becattini et al [88]. This lends some weight to the accuracy of the model when fitting particle ratios in a limited kinematic region. This grand canonical model includes the factor $\gamma_S \neq 1$ to predict the yields of strange particles. To differentiate between canonical strangeness suppression, and suppression of strange particles by anomalous phase space occupancy[13], the yield of the ϕ particle could be used. Yields of this particle are not sensitive to canonical strangeness suppression, but as it contains an s and an $\overline{s}$ quark, these yields will be sensitive to $\gamma_S \neq 1$.

The enhancement of strange particles measured by CERN WA97 has been considered a signal for QGP formation by many of the models mentioned in Chapter 2. At first glance, the ability of a full equilibrium thermal model to reproduce the data agrees with this assumption, since, as has been explained in Chapter 1, equilibrium strange particle yields have been proposed as a possible signal for deconfinement. A deconfined phase is not, however, expected to be formed in the p+Be system, as it is only expected in large dense systems. The ability of the model to reproduce the p+Be data suggests that either a deconfined phase is formed in this small system, or that it is possible for strange particles to reach equilibrium yields by hadronic interactions alone.

The usefulness of the interaction volume parameter introduced by Hamieh et al. [50] may only be investigated when 4π data becomes available. It does not appear to be necessary, and has been introduced chiefly to account for the anomalous p+Pb data point. The parameters required to describe this point have been excluded from further analysis for the reasons stated in the

[13] parameterised by $\gamma_S \neq 1$ in thermal models

text.

It has further been shown that the corrections due to canonical strangeness conservation for particles of strangeness S are not greatly affected by including, in the formalism for exact strangeness conservation, particles of strangeness $> S$.

If one were to consider the status of proposed signals of deconfinement for Pb+Pb collisions at 158 A GeV from Chapter 2, it seems likely that a deconfined phase has been formed in these collisions. Regardless, particle multiplicities are described by their equilibrium thermal values, and the enhancement of strange particles at CERN WA97 for large systems relative to p-Be is easily explained by this model of exact strangeness conservation.

Appendix A

Kinematic Variables

A.1 Baryon Stopping

At ultra-relativistic energies (greater than 10 A GeV [92]) the type of collision occurring may be divided into two broad categories:

Baryon Stopping Region: In this region the baryons in the target and projectile are partially or fully stopped by each other, forming baryon-rich matter in the interaction region of the collision [92].

Transparent Region: In this region the baryons of the target and projectile nuclei pass through each other, leaving behind a baryon-poor interaction region. There is still a large amount of energy deposited in the interaction region in this case.

The boundary between these two regions is not clearly defined. There is almost complete stopping in reactions with S and Si projectiles up to 60 A GeV. In the centre-of-mass system, the energy range for stopping is $\sqrt{s} \approx 5 - 10$ GeV per nucleon, and a totally transparent collision will have energy per nucleon of approximately $\sqrt{s} > 100$ GeV [6]. If a plasma is formed in a collision with a high degree of stopping, it will be baryon-rich. A plasma formed in the transparent region will be baryon-poor, and is expected to be similar to conditions present during the early universe. Figure A.1 shows expected net proton distributions for various cases.

A.2 Centrality

In general, the type of projectile and target used in accelerator experiments vary from proton – proton, through to Pb+Pb. An interesting variable is

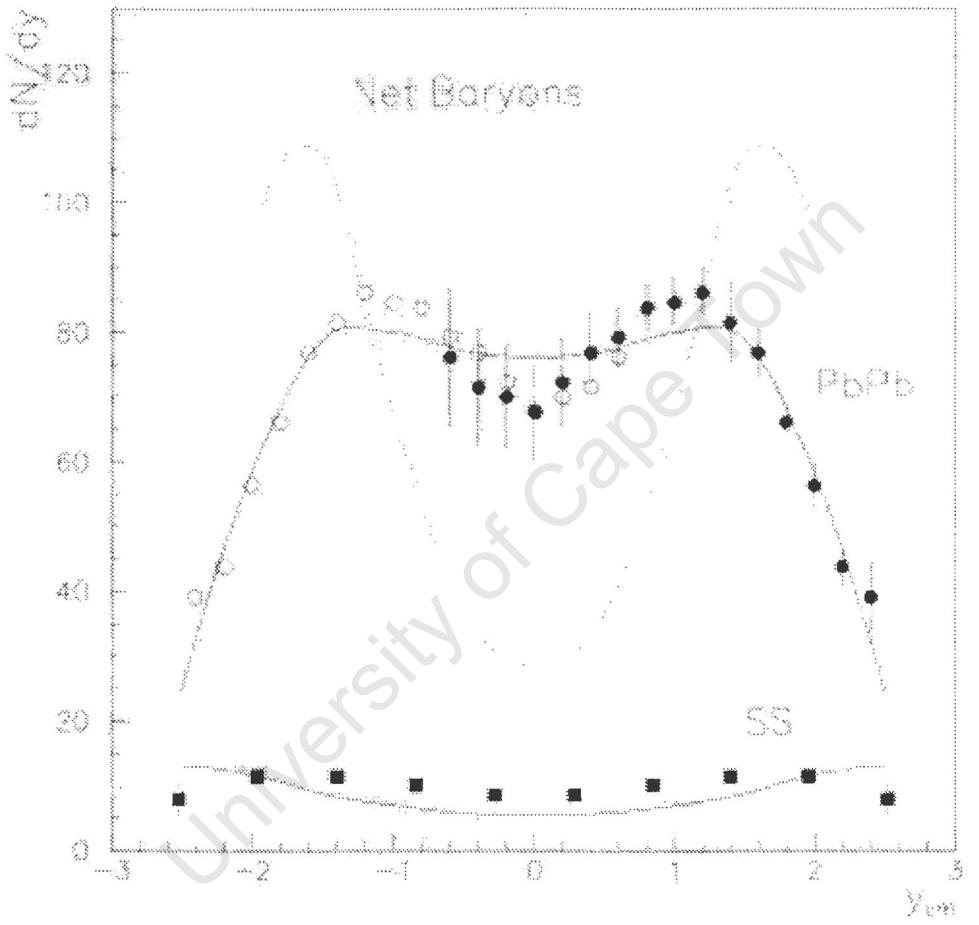

Figure A.1: Net proton distributions with (solid line) and without (dashed line) stopping [93].

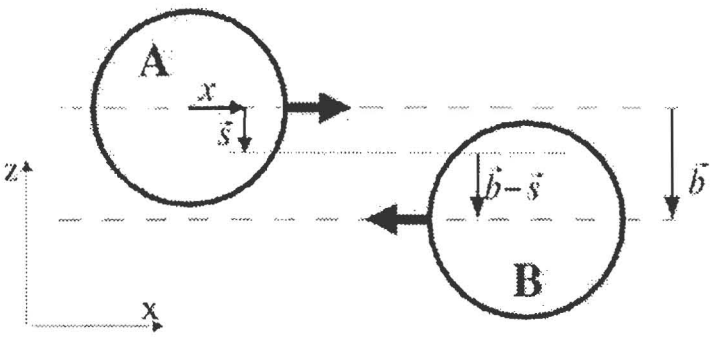

Figure A.2: A schematic representation of a collision. As b increases, the collision becomes more peripheral. The most central collision will be at b=0 [58].

that of the number of participants in the collision. With the heavier nuclei (like Pb, S, and Si), a collision may not be central (i.e. the collision may be glancing rather than head-on). The number of participants refers to the number of nucleons from either nucleus which interact with at least one nucleon of the other nucleus involved in the collision. In the most central collisions of symmetric systems (i.e. Pb+Pb, S+S), the maximal number of participants is twice the atomic number of the projectile / target. The most peripheral collisions will then have only two participants. There are various ways of estimating the number of wounded nucleons in an experiment and, hence, the centrality. The WA97 and NA57 experiments at CERN made use of the Wounded Nucleon Model [94] for Pb+Pb collisions [95]. For the p+Be and p+Pb collisions the number of wounded nucleons was calculated within the framework of the Glauber model [6, 96]. The more central a collision, the higher the proportion of initial longitudinal kinetic energy that is deposited in the interaction region.

A.3 Rapidity and Pseudorapidity

A.3.1 Rapidity

A useful variable when analysing data from a collision system is the rapidity, defined as:

$$y = \frac{1}{2} \ln \left(\frac{E + p_L}{E - p_L} \right) \tag{A.1}$$

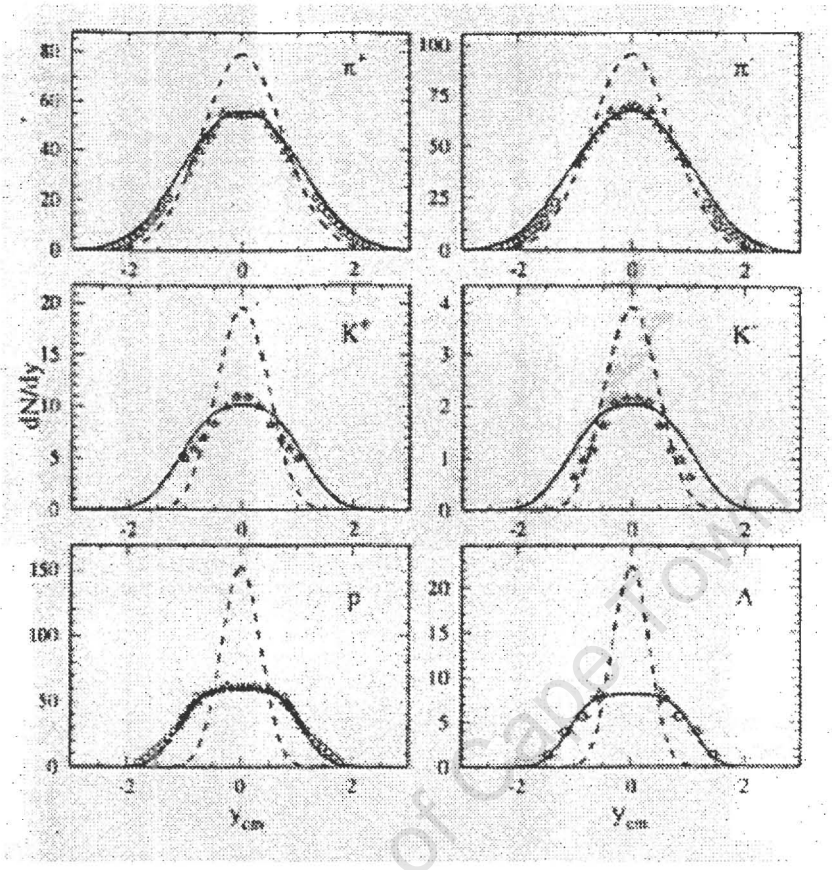

Figure A.3: Comparison of expected rapidity distributions, with (solid lines) and without (dashed lines) longitudinal flow to experimental data [89].

Where E is the energy of the particle and p_L is the particle's momentum along the direction of the beam axis. Particle numbers (multiplicities) are usually represented in rapidity bins, with the number of particles within a given rapidity range, or at a given rapidity value, plotted against rapidity itself. The higher a particle's rapidity, the greater the portion of it's energy attributed to longitudinal motion. The rapidity spectrum of a symmetric collision whose centre-of-mass (c.m.) is stationary in the laboratory frame will be centred on $y = 0$, and will be symmetric about this point. Thus, quite often only one half of the spectrum is measured. A change in the centre-of-mass momentum of the collision system with respect to the lab frame manifests itself as a linear shift of the rapidity spectrum, with no change in shape. Thus, whatever frame of reference the rapidity spectrum is measured in, it may always be transformed to the centre-of-mass frame by a simple linear shift of the centre of the spectrum to $y = 0$.

Rapidity may be considered the relativistic variable analogous to classical velocity or momentum, as a high rapidity implies a large longitudinal momentum and rapidity transforms from one relativistic frame to another according to the Galilean velocity transformations (addition of a constant). The mid-rapidity region is the region between the target and projectile rapidities. Most newly produced particles may be found in this central rapidity region in symmetric collisions.

A.3.2 Pseudorapidity

At large energies ($E \to \infty$) the energy term in the definition of rapidity above may be replaced by the magnitude of the 3-momentum vector which also approaches infinity ($|\vec{p}| \to \infty$). This substitution gives the definition of pseudorapidity (η):

$$\eta = \frac{1}{2} \ln \left(\frac{|\vec{p}| + p_L}{|\vec{p}| - p_L} \right) \tag{A.2}$$

At large energies, the pseudorapidity and rapidity variables are approximately the same. In the region of $\eta \approx 0$, there is a dip in the particle multiplicity compared to the rapidity value. The peak of the pseudorapidity distribution is smaller than that of the rapidity distribution by approximately $(1 - \frac{m_0^2}{<m_T^2>})$[1] [6].

A.3.3 Longitudinal Flow

The rapidity distribution predicted assuming a Boltzmann distribution for massive particles emitted by a stationary thermal source, appears as a Gaussian, centred at $y = 0$ in the centre-of-mass frame of width [90]:

$$\Gamma_{\text{fwhm}} = \sqrt{8 \ln 2 \frac{T}{m_0}} \approx 2.35 \sqrt{\frac{T}{m}} \tag{A.3}$$

For massless particles, the width of the rapidity distribution is expected to be [90]:

$$\Gamma_{\text{fwhm}} \approx 1.76 \tag{A.4}$$

All measured rapidity spectra show widths in excess of those described in Equation (A.3). This indicates that particles exhibit some memory of the momenta of the initial colliding nuclei. A first attempt at describing this effect by including non-thermal resonance decay particles was unsuccessful as

[1] m_T and m_0 are described in Appendix A.4

this had the effect of narrowing the width of the expected rapidity spectrum [91]. In the Bjorken model for asymptotically high energies [4], and complete nuclear transparency, rapidity distributions are predicted to be extended constant plateaus as opposed to the Gaussians predicted for a stationary thermal source. With experimental data exhibiting a behaviour between that of these two extremes, an intermediate theory is expected to describe the data. To account for widths of rapidity spectra from CERN SPS, the assumption of some type of partial nuclear transparency or incomplete stopping, leading to a large longitudinal flow of the thermal system along the beam axis, is utilised. The magnitude of this flow may increase with distance along the z axis from the the centre-of-mass, where the system is considered to be at rest (in the longitudinal direction).

The limited available beam energy and potential stopping observed in the colliding system is accounted for by restricting the rapidity interval of the Bjorken model to between that of the projectile and target rapidity regions (or y_{min} and y_{max}) [90]. This makes it possible to reproduce the experimentally observed rapidity spectra, as seen in Figure A.3.

A.4 Transverse mass (m_T), Transverse momentum (p_T), and m_T-scaling

The transverse mass of a particle detected after a collision is defined as:

$$m_T = \sqrt{{m_0}^2 + {p_T}^2} \tag{A.5}$$

Where m_0 is the rest mass of the particle, and p_T is the particle's momentum in a direction transverse to the beam axis. A stationary thermal Boltzmann source, at large values of the transverse mass, is expected to behave according to:

$$\lim_{m_T \to \infty} \frac{1}{m_T^{3/2}} \frac{dN}{dm_T} \propto e^{\frac{-m_T}{T}} \tag{A.6}$$

This behaviour of the system is described as 'm_T-scaling'. For a small rapidity window it is more useful to plot [90]:

$$\frac{1}{m_T} \frac{dN}{dy dm_T} \propto e^{\frac{-m_T}{T_{\text{eff}}}} \tag{A.7}$$

Where in this case, T_{eff} is given by:

$$T_{\text{eff}} = T/\cosh(y - y_I) \tag{A.8}$$

Where y_I is the rapidity of what would be $y = 0$ in the centre-of-mass frame, given by the centre of the peak of the rapidity distribution. Particles emitted by resonance decays are not expected to exhibit m_T-scaling, as they may be formed outside the interaction volume, or not have had time to reach equilibrium. This is apparent when observing the low p_T tail on, for example, the pion spectra – of which a large contribution comes from resonance decays . This can be seen in Figure A.4 with the h^- data, to which the largest contribution is from pions.

A.4.1 Transverse Flow

As shown in Figure 2.4, the inverse slope parameter (T) displays a mass dependence for all particles, except the multi-strange hadrons. Assuming a global transverse velocity (v_T) for the system, the transverse momentum of each particle species is boosted according to:

$$p_{T_{\text{eff}}} = p_T + m_0 v_T \tag{A.9}$$

This seems to accurately describe the data. The p_T-spectra of all particles are modified according to their mass, increasing the apparent temperature of heavy particles more than that of the lighter particles. This effect is enhanced at low p_T values and, in the limit of large p_T ($p_T >> m$), may be ignored, with all particles again exhibiting the same temperature parameter.

For a system with universal transverse expansion, at large p_T, T needs to be replaced by T_{exp}, the effective temperature given by [90]:

$$T_{\text{exp}} = T\sqrt{\frac{1 - v_T}{1 + v_T}} \tag{A.10}$$

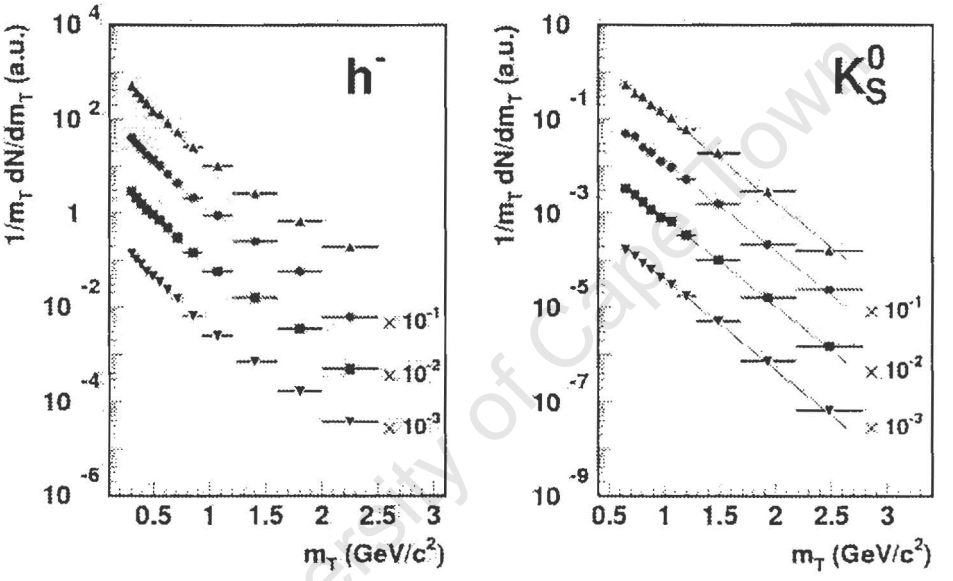

Figure A.4: m_T-spectra from CERN WA97 for negatives, and the K^0_S [55]. The K^0_S shows m_T-scaling. The h^- only exhibit m_T-scaling for m_T greater than 1 GeV/c^2.

Appendix B

The Acceptance Region of WA97 for Pb+Pb collisions

As an example of the acceptance region of the CERN WA97 experiment, I present here the acceptance of the detectors for the Pb-Pb collisions.

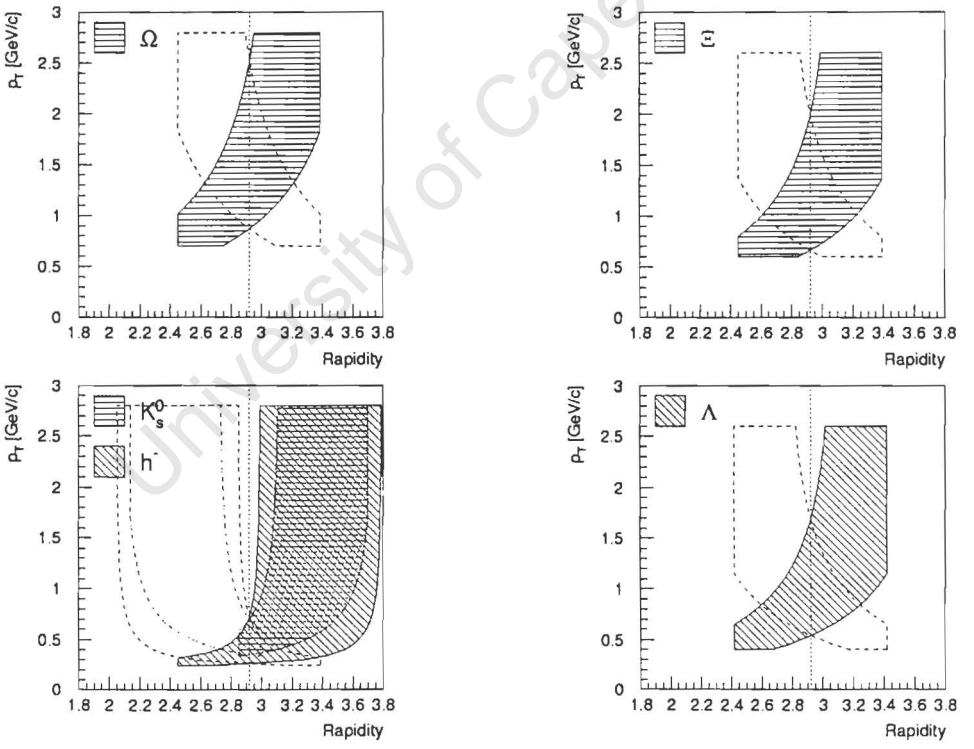

Figure B.1: The CERN WA97 acceptance regions for Λ, Ξ, Ω, $K^0{}_S$, and h^- particles formed by Pb+Pb collisions [55].

The shaded areas of Figure B.1 give the acceptance for the various par-

ticles. The dashed lines show reflection about mid-rapidity ($y = 2.91$).

Bibliography

[1] E. Shuryak, *Sov. J. of Nucl. Phys.* **28** (1978) 408; *Phys. Rep.* **61** (1980) 72.

[2] F. Karsch **hep-ph/0103314 v1** (2001).

[3] M. C. Abreu, *et al.*, *Phys. Lett.* **B447** (2000).

[4] J. D. Bjorken, *Phys. Rev.* **D27** (1982) 140.

[5] U Heinz, **nucl-th/9810056 v2** (1999).

[6] C. Y. Wong, *Introduction to High-Energy Heavy-Ion Collisions* (World Scientific Publishing, Singapore 1994) 251 - 264 and references therein.

[7] S. M. Wheaton, Unpublished - MSc. Thesis (2001).

[8] C. Gale **hep-ph/0104235 v2** (2001).

[9] T. Peitzmann **nucl-ex/0009014 v1** (2000).

[10] D. H. Perkins, *Introduction To High Energy Physics* (2nd Edition Addison – Wesley Publishing Company. England, 1982).

[11] M. Masera, *Nucl. Phys.* **A590** (1995) 93c.

[12] P. Bordalo, *Nucl. Phys.* **A661** (1999) 538c.

[13] D. K. Srivastava, talk given at QM 2001, (2001).

[14] P. Aurenche, F. Gelis, H. Zaraket, R. Kobes, *Phys. Rev.* **D58** (1998).

[15] D. K. Srivastava, *Eur. Phys. J.* **C10** (1999) 487.

[16] M.M. Agarwal, *et al*, *Phys. Rev. Lett.* **85** (2000) 3595.

[17] D. K. Srivastava and B. Sinha *Phys. Rev.* **C64** (2001) 034902.

[18] F.D. Steffen and M.H. Thoma **hep-ph/0103044 v2** (2001).

[19] T. Matsui and H. Satz, *Phys. Lett.* **B178** (1986) 416.

[20] M.I. Gorenstein, **hep-ph/0011304 v2** (2000).

[21] J. Qiu, *et al*, **nucl-th/0106040 v1** (2001).

[22] R. Arnaldi, **hep-ex/0106079 v1** (2001).

[23] D. Prorok, **hep-ph /0107260** (2001).

[24] R. Hanbury-Brown and R. Q. Twiss, *Phil. Mag.* **45** (1954) 633.

[25] S.Y. Fung, *et al*, *Phys. Rev. Lett.* **41** (1978) 1592.

[26] S. Pratt, *Phys. Rev.* **D33** (1986) 72.

[27] Y. Hama, S.S. Padula, *Phys. Rev.* **D37** (1998) 3237.

[28] G. F. Bertsch, *Nucl. Phys.* **A498** (1989) 173c.

[29] C. Adler, *et al*, (Star Colaboration), **nucl-ex/0107008 v1** (2001).

[30] S. Soff, *et al*, **nucl-th/0012085 v2** (2001).

[31] J. Rafelski and B. Muller, *Phy. Rev. Lett.* **48** (1982) 1066.

[32] P. Koch, B Muller and J. Rafelski, *Phys. Rev.* **D34** (1986) 783.

[33] J.W. Harris and B. Muller, **hep-ph/9602235 v2** (1996).

[34] T. Abott, *et al.*, E802 collaboration, *Phys. Rev. Lett.*]textbf55 (1991) 1567; W. A. Zajc, *et al.*, E802 collaboration, *Nucl. Phys.* **A544**.

[35] C. M. Ko, L. Xia, *Phys. Rev.* **C38** (1988) 179.

[36] C.M. Ko, L. Xia,]textitNucl. Phy. **A498** (1989) 561c.

[37] J. Cleymans, H. Oeschler, K. Redlich, *Phys. Lett.* **B485** (2000) 27.

[38] W. Cassing **nucl-th/9906072 v1** (1999).

[39] H.Sorge, **nucl-th/9707021 v1** (1997).

[40] NA44 Collaboration, **nucl-ex/9907013** (1999).

[41] P. Braun-Munzinger, *et al*, **hep-ph/0106066** (2001).

[42] F. Wang, **nucl-ex/9905005** (1999).

[43] J. Rafelski, *et al.*, **hep-ph/9910300** (1999).

[44] D. Rohrich, **hep-ex/9607005** (1996).

[45] J. Rafelski, *et al*, *Acta Physica Polonica* **B27** (1996) No.5.

[46] J. Rafelski, *et al.*, **hep-ph/0104132** (2001).

[47] J. Cleymans, K. Redlich, E. Suhonen, *Z fur Physik* **C51** (1990) 137.

[48] A. Muronga, J Cleymans, *Phys. Lett.* **B388** (1996)

[49] J. Cleymans, M. Marais, *Phys. Rev.* **C56** (1997) 2747.

[50] S. Hamieh, K. Redlich, A. Tounsi, *Phys. Lett.* **B486** (2000) 61.

[51] R. Hagedorn, K Redlich, *Z. fur Physik* **C27** (1985) 541.

[52] F. Antinori, *et al*, *Nucl. Phys.* **A590** (1995) 139c.

[53] E. Anderson, *et al*, *Phys. Lett.* **B433** (1998) 209.

[54] D. Rohrich *J. of Physics* **G27** (2001) 355.

[55] F. Antinori, *et al.*, *Eur. Phys. J.* **C14** (2000) 633.

[56] D. Elia, *et al.*, *Proceedings of QM99* (1999).

[57] R. Caliandro, *et al.*, *J. of Phys.* **G25** (1998).

[58] F. Antinori, *et al.*, *Eur. Phys. J.* **C18** (2000) 57.

[59] F. Antinori, *et al.*, *Nucl. Phys.* **A661** (1999) 130c.

[60] A Dumitru, *et al*, **nucl-th/9901046** (1999)

[61] E Andersson, *et al*, *Phys. Lett.* **B449** (1999) 401.

[62] Cern Web - Site, **http://www.cern.ch.**

[63] F. Antinori, *et al.*, *Eur. Jour. Phys.* **C11** (1999) 79.

[64] K. Werner, *Phys. Rep.* **232** (1993) 87.

[65] H. Sorge, *Phys. Rev.* **C52** (1995) 3291.

[66] A Bialas, *et al*, *Nucl. Phys.* textbfB111 (1976) 461.

[67] R. Brun, *et al*, **GEANT3**, CERN program library Q123.

[68] S. Soff, *et al*, **nucl-th/9907026** (2000).

[69] S. A. Bass, *et al.*, **nucl-th/9803035 v2** (1998).

[70] N.S. Amelin, *et al*, **hep-ph/0012276** (2000).

[71] S. Ben-Hao, *et al*, **hep-ph/9904436** (1999).

[72] H. Pi, *Comp. Phys. Commu.* **90** (1995) 121.

[73] B Andersson, *Phy. Lett B256* **337** (1991).

[74] A. Capella, C.A. Salgado, **hep-ph/9903414** (1999)

[75] A. Capella, *et al*, *Phys. Lett.* **B81** (1979) 68.; *Phys. Rep.* **236** (1994) 235..

[76] S. E. Vance, M Gyulassy, **nucl-th/9901009** (1999).

[77] D. Kharzeev, *Phys. Lett.* **B378** (1996) 238.

[78] G.C. Rossi, G. Veneziano, *Nucl. Phys.* **B123** (1977) 507.

[79] A. Kerrannen, F Beccattini, **Talk given at workshop in Trento** (2001).

[80] J. Rafelski, *Phys. Lett.* **262** (1991) 333.

[81] C. Slotta, *et al.*, *AIP Conf. Proc.* **340** *Strangeness in Hadronic Matter* (1995) 462.

[82] M. Abramowitz, I.A. Stegun, *Handbook of Mathematical Functons with Formulas, Graphs, and Mathematical tables* New York: Dover (1965).

[83] J. Cleymans, K. Redlich, *Phys. Rev.* **C60** (1999).

[84] G. D. Yen, M. I. Gorenstein, **nucl-th/9808012 v3** (1999).

[85] J. Sollfrank, *et al*, *Z. Phys.* **C61** (1994) 659.

[86] R. Barton, *et al*, *J. Phys.* **G27** (2001) 367.

[87] D.E. Groom, *et al*, *Eur. Phys. Journ.* **C15** (2000).

[88] F. Becattini, *et al.*, *Phys. Rev.* **C63** (2001) 649.

[89] J. Stachel, *Nucl. Phys.* **A610** (1996) 509c.

[90] D. M. Elliott, *MSc. Thesis* University of Cape Town (1996)

[91] E. Schedermann, J. Sollfrank and U. Heinz, *Phys. Rev.* **C48** (1993) 2462.

[92] L.P. Csernai, *Introduction To Relativistic Heavy Ion Collisions*, John Wiley and Sons Ltd. (1994).

[93] A. Capella, **hep-ph/9910219** (1999)

[94] A. Bialas, M. Bleszynski, W. Czyz, *Nucl. Phys.* **B111** (1976) 461.

[95] N. Carrer, *J. Phys.* **G27** (2001) 391.

[96] D. Rohrich, *J. Phys.* **G27** (2001) 355.

[97] F. Cooper, G. Frye, *Phys. Rev.* **D10** (1974) 186.

[98] R. K. Pathria, *Statistical Mechanics*,Butterworth - Heinemann, England (1996) 495.

[99] F. Becattini, *Hadrons in Dense Nuclear Matter and Hadrosysthesis - Proceedings* (1998) 72.

[100] E Suhonen, *et al*, *Hadrons in Dense Nuclear Matter and Hadrosynthesis - Proceedings* (1998) 235.

[101] J. Cleymans, *et al*, *Phase structure of Strongly Interacting Matter - Proceedings* (1990).

[102] H. van Hecke, *et al*, *Phys. Rev. Lett.* **81** (1998).

Acknowledgements

I would like to thank:

Prof. Jean Cleymans: for his assistance, and the wealth of knowledge he has provided.

Dr. Roger Fearick: for help with computational matters.

Spencer Wheaton: for his painstaking efforts at proof reading and a number of stimulating conversations.

Mark Horner: for stimulating conversations over the past 6 years, and help with computational problems.

Bruce Becker: for many bottles of Jack, accompanied by stimulating conversation. Also for help with Gnuplot – The most kick ass plotting programme around.

The National Research Foundation: for providing financial support towards my MSc. studies.

The Organising Committee of Strangeness 2000: for enabling me to attend the Strangeness 2000 conference at the University of California, Berkeley.

My Parents: who have been encouraging, and supportive throughout my academic career and whom I love very much.